Received: 21 July 2018 | Revised: 17 December 2018 | Accepted: 19 December 2018

DOI: 10.1002/qj.3465

RESEARCH ARTICLE

Quarterly Journal of the Royal Meteorological Society RMetS

Understanding the dissipation of continental fog by analysing the LWP budget using idealized LES and *in situ* observations

Eivind G. Wærsted[1] | Martial Haeffelin[2] | Gert-Jan Steeneveld[3] | Jean-Charles Dupont[4]

[1]Laboratoire de Météorologie Dynamique, École Polytechnique, Université Paris-Saclay, Palaiseau, France
[2]Institut Pierre Simon Laplace, École Polytechnique, CNRS, Université Paris-Saclay, Palaiseau, France
[3]Meteorology and Air Quality section, Wageningen University, Wageningen, The Netherlands
[4]Institut Pierre Simon Laplace, École Polytechnique, UVSQ, Université Paris-Saclay, Palaiseau, France

Correspondence
Eivind G. Wærsted. Laboratoire de Météorologie Dynamique, École Polytechnique, Université Paris-Saclay, Route de Saclay, 91128 Palaiseau, France.
E-mail: ewaersted@lmd.polytechnique.fr

Funding information
Direction Générale de l'Armement (France), Meteomodem and the Netherlands Organization for Scientific Research (contract 863.10.010 and project number SH-312-15),

Physical processes relevant for the dissipation of thick, continental fog after sunrise are studied through observations from the SIRTA observatory and idealized sensitivity studies with the large-eddy simulation model DALES. Observations of 250 fog events over 7 years show that more than half of the fog dissipations after sunrise are transitions to stratus lasting 2 hr or more. From the simulations, we quantify the contribution of each process to the liquid water path (LWP) budget of the fog. Radiative cooling is the main source of LWP, while surface turbulent heat fluxes are the most important process contributing to loss of LWP, followed by the absorption of solar radiation, the mixing with unsaturated air at the fog top and the deposition of cloud droplets. The loss of LWP by surface heat fluxes is very sensitive to the Bowen ratio, which is importantly affected by the availability of liquid water on the surface; in a run without liquid on the surface, fog dissipation occurred 85 min earlier than in the Baseline simulation. The variability of stratification and humidity above fog top is documented by 47 radiosondes and cloud radar. Using DALES, we find that the variability in stratification has an important impact on the entrainment velocity; a three times more rapid fog-top entrainment enables the cloud base to lift from the ground 90 min earlier in weak stratification than in strong stratification in the model. With relatively dry overlying air, the fog evaporates faster than if the air is near saturation, leading to 70 min earlier dissipation in our simulations. Continuous observations of the temperature and humidity profiles of the layer overlying the fog could therefore be useful for understanding and anticipating fog dissipation.

KEYWORDS
Fog dissipation, fog, bowen ratio, fog-top entrainment, LES

1 | INTRODUCTION

Fog is defined as the presence of suspended water droplets in vicinity of the surface, generally reducing the horizontal visibility to below 1 km (American Meteorological Society, 2012). Fog can form in most parts of the world, by a large number of different mechanisms depending on location and season (Gultepe *et al.*, 2007). Fog may cause severe delays in traffic, in particular at airports, due to the necessary precautions in low visibility conditions (Gultepe *et al.*, 2009). Predicting when and where fog will form, as well as the time of dissipation, is therefore an important objective for atmospheric sciences. Since fog formation depends on a subtle balance between many processes which may vary locally, fog has proven very challenging to forecast precisely with regional-scale numerical weather models (e.g. Steeneveld *et al.*, 2015).

To improve fog forecasts for a specific site, e.g. an airport, nowcasting tools have been developed based on the statistical analysis of many years of surface meteorological observations at the site, to forecast visibility in the near future (e.g. Pasini *et al.*, 2001; Román-Cascón *et al.*, 2016). In order to extend such tools to more sophisticated observations such as vertical profilers (e.g. ceilometers, cloud radars), understanding of the physical processes responsible for the evolution of the fog is required to optimize the use of the profilers. These remote-sensing instruments may detect phenomena that occur at a higher altitude than where the surface observations are

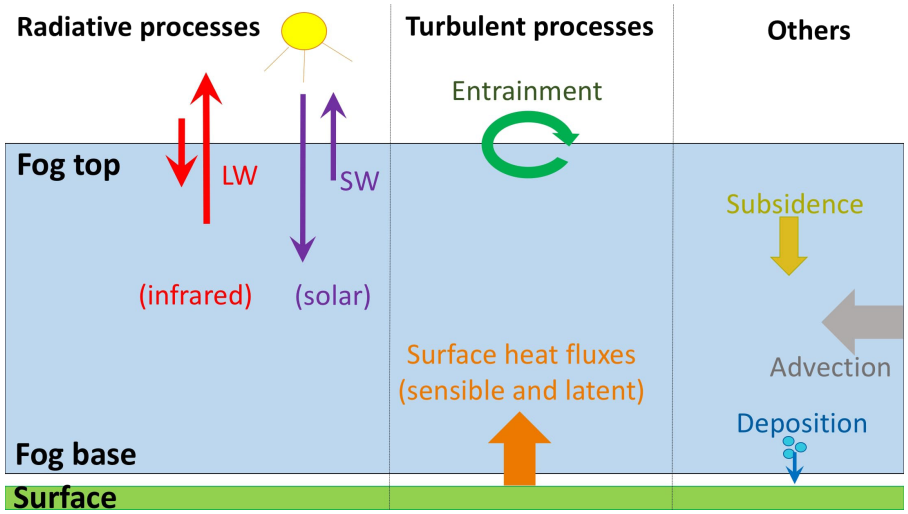

FIGURE 1 Schematic of the fog layer and the local processes that affect its liquid water content [Colour figure can be viewed at wileyonlinelibrary.com]

taken; for example, ceilometers may detect the hygroscopic growth of aerosols at up to a few hundred metres altitude, which often precedes fog formation (Haeffelin *et al.*, 2016).

The dissipation of continental fog after sunrise is an interaction of many physical processes. Although fog often dissipates after sunrise due to heating caused by solar radiation, the time of dissipation can be very variable (section 2.2). The persistence of fog depends on the presence of suspended liquid water near the surface. Fog dissipation may occur through a complete depletion of the liquid layer, but also through a transition of the fog into low stratus cloud, since both these scenarios will increase the visibility at screen level. While the first scenario requires a complete depletion of the fog liquid water path (LWP), the second only requires a vertical displacement of the liquid water and may occur without a strong decrease in LWP. This paper explores the local processes which affect these two mechanisms.

The local processes affecting the fog layer are shown schematically in Figure 1. Radiative cooling at the fog top is the main source of LWP (Brown and Roach, 1976; Wærsted *et al.*, 2017), while many processes contribute to removal of LWP, notably the heating of the fog or underlying surface by solar radiation (Brown and Roach, 1976; Haeffelin *et al.*, 2010; Wærsted *et al.*, 2017), the mixing of the fog with warm, dry air above its top (Gultepe *et al.*, 2007), or the deposition of droplets on the surface or canopy (Katata, 2014). Also indicated on the figure is "Advection", which represents all the processes that depend on horizontal heterogeneity, advection of synoptic phenomena and other non-local effects. These can impact fog importantly, but are not investigated in this paper.

Previous papers have applied large-eddy simulations (LESs) to study the impacts of local processes in fog. They have focussed on the turbulent structures during phases of radiation fog (Nakanishi, 2000; Bergot, 2013; 2016), fog-layer deepening and transition from stable to adiabatic fog (Porson *et al.*, 2011), the impact of cloud condensation nuclei concentrations on the fog life cycle through radiative and microphysical processes (Maalick *et al.*, 2016; Mazoyer *et al.*, 2017), and the impact of the wind speed (Bergot, 2016; Maronga and Bosveld, 2017). However, certain other aspects have received less attention, especially the properties of the air overlying the fog. Another aspect which has received little attention is the water on top of the vegetation; while the effect of the soil moisture was studied by Maronga and Bosveld (2017), the impact of water present on the surface itself was not treated.

In this paper, the following research questions are posed:

(a) How much does each local process contribute to the LWP budget of the fog?
(b) What is the impact of the presence of liquid water at the surface on fog dissipation?
(c) What is the impact of the temperature and humidity profiles above the fog top on fog dissipation?

To answer these questions, we perform idealized sensitivity studies with LES on an observed fog event. The aim is not primarily to reproduce this particular event, but rather to understand the contributions of various local processes and how sensitive they are to boundary conditions. To quantify the contribution from each process to the tendency in fog LWP, we use a novel approach of model output analysis (section 3.3). The impact of the stratification and humidity above fog top is studied by performing sensitivity studies that span the variability of these properties observed by 47 radiosondes.

The paper is structured as follows: In section 2, we describe the dataset of fog observations and some statistics which are used as a basis for the sensitivity studies. In section 3, the LES model and the set-up of each simulation are described, as well as the LWP budget analysis method. The results of the simulations are presented in section 4, together with a discussion of their implications. Conclusions and outlook are presented in section 5.

FIGURE 2 Photo of the SIRTA main facility, where all observations used in this study are taken, apart from the radiosondes. The distance from the tree line to the road is about 80 m, and from the tree line to the lake it is 200 m [Colour figure can be viewed at wileyonlinelibrary.com]

2 | OBSERVATIONS OF FOG AT THE SIRTA OBSERVATORY

2.1 | The observational dataset

The multi-instrumental atmospheric observatory SIRTA (Site Instrumental de Recherche par Télédétection Atmosphérique) has continuously recorded a large number of atmospheric variables since 2002 (Haeffelin *et al.*, 2005). This site (48°43′N, 2°12′E) is well suited for the study of fog due to the relatively high number of days with fog (about 30 per year), and fog has been a prioritized topic of study since 2006, when the ParisFog project started (Haeffelin *et al.*, 2010). In this paper, several observations from the SIRTA main facility are used to study statistics of atmospheric state during many fog events, and to initialize and evaluate the LES model for a specific event (Table 1). The site is located 156 m above sea level in a suburban area about 20 km south of Paris city centre with patches of grass, forest and built-up areas. All the instruments are deployed in an area smaller than 200 m in diameter, apart from the radiosondes. The closest surroundings are an open field, with a line of trees to the north and a small lake to the south (Figure 2). The surrounding trees have been shown to impact turbulence in stable conditions and to delay the time of fog formation (Mazoyer *et al.*, 2017), and the lake is associated with a permanent shallow water table, giving high soil moisture locally at the site (Campoy *et al.*, 2013).

The visibility observed at 4 m is used to detect fog, while the visibility at 20 m is used to determine when the fog is thicker than 20 m. The environment of the fog is further characterized by the air temperature recorded at six levels on a 30 m mast, the skin temperature measured by an unshielded probe on top of the soil in the grass field, the soil temperature and moisture measured at six depths, and the wind profile up to 200 m observed by sonic anemometers and a sodar. The different terms of the surface energy balance are also measured: short-wave (SW) and long-wave (LW) radiative fluxes at 10 m, turbulent sensible and latent heat fluxes at 2 m (eddy covariance method), and soil heat flux at 5 cm depth.

Full atmosphere profiles of temperature and humidity are available around 0000 and 1200 UTC from radiosondes launched from the Météo-France station Trappes, which is located 15 km to the west of SIRTA and 12 m higher.

The Vaisala CL31 ceilometer (Kotthaus *et al.*, 2016) is used to detect the cloud-base height (CBH) of the fog cloud, when it is not touching the ground, using the threshold value of $2 \times 10^{-4}\,\mathrm{m^{-1}sr^{-1}}$ in the attenuated backscatter, following Haeffelin *et al.* (2016). Above the cloud base, the ceilometer signal is rapidly attenuated, preventing further information about the cloud beyond its base to be obtained. To observe the profile of the cloud and detect its top, the 95 GHz cloud radar BASTA (Bistatic rAdar SysTem for Atmospheric studies) is used (Delanoë *et al.*, 2016). This cloud radar uses the frequency-modulated continuous wave (FMCW) technique, which requires much smaller emitted power than traditional pulsed radars, making its components less expensive. Its small blind-zone (40–60 m) and high vertical resolution (12.5 m) makes it well suited for fog studies. The average cloud top (e.g. in a 10 min period) is set to the highest cloud radar gate where at least half the measurements are retained after the automatic noise filtering algorithm of the cloud radar (Delanoë *et al.*, 2016). Finally, the multi-wavelength microwave radiometer (MWR) HATPRO (Humidity And Temperature PROfiler) is used to retrieve the LWP of the atmospheric column and the temperature profile up to 10 km. The uncertainty of the LWP product is $\pm 20\,\mathrm{g/m^2}$ according to the manufacturer, but for relatively small LWP ($<40\,\mathrm{g/m^2}$) investigations indicate that the uncertainty is only ± 5–$10\,\mathrm{g/m^2}$, at least when the fog forms in clear sky so that a possible time-independent bias can be corrected for (Marke *et al.*, 2016; Wærsted *et al.*, 2017). The MWR temperature profile only has 4–5 degrees of freedom, limiting

TABLE 1 Overview of the observations used in this study. All observations are taken in the SIRTA observatory main facility, except the radiosondes which are launched at Trappes (15 km to the west of SIRTA). The column "Used for" indicates those observations used for initialization of the model (I), for comparison with the model (C) and for the analysis on an extended dataset (presented in sections 2, 4.3) (A)

Instrument	Measured quantity	Used for	Vertical range and resolution	Temporal resolution
Remote sensing				
95 GHz Doppler FMCW cloud radar (LATMOS, BASTA)	Radar reflectivity (dBZ)	I,C,A	RA 0.05–6 km, RE 12.5 m	12 s
14-channel microwave radiometer (RPG HATPRO)	Liquid water path (g/m^2) Temperature profile (K)	I,C I,A	Integrated RA 0–10 km, 4–5 deg. of freedom	60 s $\approx$ 5 min
905 nm Ceilometer (Vaisala CL31)	Attenuated backscatter (m^{-1} sr^{-1})	C,A	RA 0–7.6 km, RE 15 m	30 s
Sodar (Remtech SFAS)	Wind speed profile (m/s)	I	RA 10–200 m, RE 5 m	10 min
Surface layer state				
550 nm scatterometer (Degreane DF320)	Visibility (m)	C,A	At 4 m	60 s
875 nm scatterometer (Vaisala PWD22)	Visibility (m)	A	At 20 m	60 s
Thermometers (Guilcor PT100)	Air temperature (K)	I,C	At 1, 2, 5, 10, 20, 30 m	60 s
Barometer (Vaisala PTB110)	Surface pressure (Pa)	I	At 2 m	60 s
Sonic anemometers (METEK)	Mean wind speed (m/s)	I	At 10,30 m	10 min
Ground and soil state				
Thermometer (unsheltered PT100 probe)	Skin temperature (K)	I,C	At ground level	60 s
Soil thermometer (Guilcor PT100)	Soil temperature (K)	I	At 5, 10, 20, 30, 50, 100 cm depth	60 s
Soil moisture sensor (ThetaProbe)	Soil moisture (m^3/m^3)	I	At 5, 10, 20, 30, 50, 100 cm depth	60 s
Surface energy balance				
Pyranometers (Kipp & Zonen CMP22)	Down- and upwelling SW irradiance (W/m^2)	C,A	At 10 m	60 s
Pyrgeometers (Kipp & Zonen CGR4)	Down- and upwelling LW irradiance (W/m^2)	C,A	At 10 m	60 s
Heat flux sensor (Hukseflux HFP01SC)	Soil heat flux (W/m^2)	C,A	At 5 cm depth	60 s
GILL sonic anemometer and LI-7200 infrared gas analyser	Sensible and latent heat flux (W/m^2)	C,A	At 2 m	10 min
Radiosondes (Meteomodem M10, Météo-France, Trappes)	Temperature (K) and relative humidity (%) profiles	I,A	RA 0–30 km, RE $\approx$ 5 m	12 hr

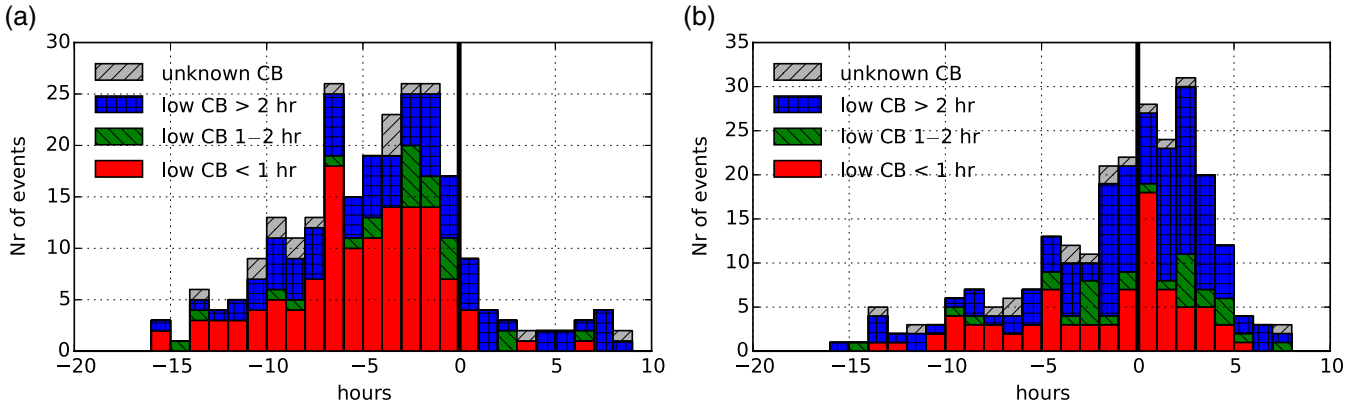

FIGURE 3 Time of (a) formation and (b) dissipation relative to sunrise of the 250 fog events at SIRTA in the period from 01 October 2010 to 30 September 2017. The different sections of the bars mark how long a cloud base (CB) is present below 400 m (in (a)) before formation and (in (b)) after dissipation, ignoring cloud absence lasting less than 30 min [Colour figure can be viewed at wileyonlinelibrary.com]

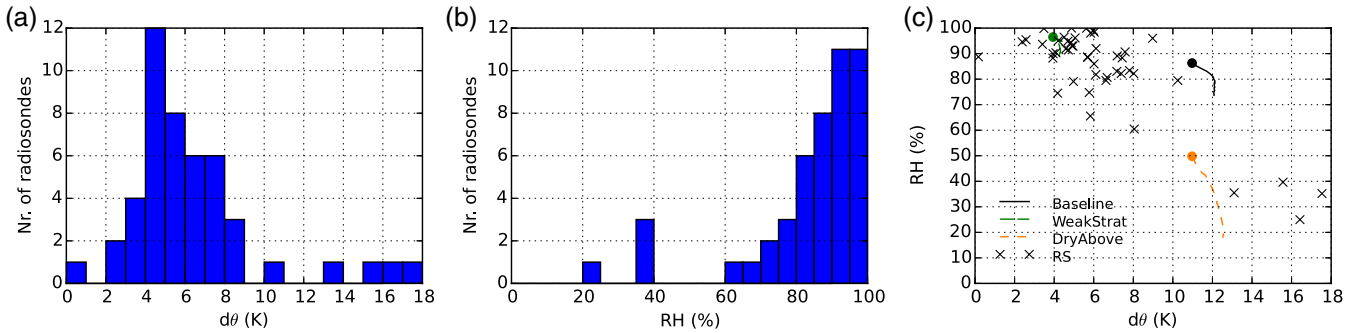

FIGURE 4 Statistics of observations of the layer above fog top. The data come from 47 radiosondes launched at Trappes near 0000 or 1200 UTC in the period from 01 October 2013 to 30 September 2017 when cloud base at SIRTA (from the ceilometer CBH product) was below 130 m and cloud top was below 600 m, and within 6 hr of a fog event at SIRTA. (a) Stratification (difference in potential temperature, dθ, from the 2 m observation at Trappes to 200 m above CTH); (b) average relative humidity in the layer 50–200 m above CTH. The CTH is determined using the cloud radar BASTA at SIRTA (except for three cases of very thin fog, where we use the visibility at 20 m). (c) The quantities shown in (a) and (b) plotted against each other (crosses). Also indicated are the initial states of three of the LES simulations performed in this paper (circles) and the evolutions in the first 3 hr of the simulations (lines) [Colour figure can be viewed at wileyonlinelibrary.com]

the details that can be retrieved from it, but with the best resolution in the lowest layer.

2.2 | Atmospheric conditions during 7 years of fog events at SIRTA

We define fog using the visibility at 4 m. Each block of 10 min is considered to be fog if more than half the visibility measurements are less than 1 km. Fog events are defined based on positive and negative constructs, similar to the method of Tardif and Rasmussen (2007). We consider periods of five consecutive 10 min blocks where the central block is a fog block: it is a positive construct if at least two other blocks also are fog blocks, and a negative construct otherwise. A fog event forms when a positive construct is encountered (the formation time is at the first fog block in that construct), and it dissipates after the last fog block in the last positive construct before either a negative construct or three consecutive non-fog blocks are encountered. Fog events separated by less than 1 hr are merged, and finally all fog events lasting less than 1 hr are discarded. This algorithm detects 250 fog events at SIRTA in the period 01 October 2010 to 30 September 2017, of which 218 occur in the winter half-year (October–March). In this section, some statistics of these fog events are presented, in order to put our simulations into context.

Figure 3 shows the formation and dissipation times of these fog events relative to the time of sunrise. The peak occurrence of fog formation is in the last few hours before sunrise, while fog dissipation most frequently occurs during the first 4 hr after sunrise. This is consistent with previous studies on radiation fog and stratus-lowering fog (Tardif and Rasmussen, 2007; Dupont *et al.*, 2016), which are the dominating fog types at this site (Dupont *et al.*, 2016). There is also an important number of events that dissipate at night, but these are often short; more than half of the events dissipating at night last less than 3 hr, while this is the case for only a quarter of the events with daytime dissipation (not shown). The classification of the histograms indicates how long a cloud base below 400 m occurs before formation and after dissipation. For some events, the category is unknown due to missing ceilometer data. Figure 3a shows that the majority of the fog events that form at night are preceded by a cloud base for less than 1 hr. This is typical for radiation fog, which forms from clear sky but may form initially at an altitude of some tens of metres,

leading to a brief period of very low cloud base before the reduction of visibility (e.g. Haeffelin *et al.*, 2016; Mazoyer *et al.*, 2017). There are also many events which have a cloud base for more than 2 hr before formation. This is interpreted as stratus-lowering fog. The fog events forming after sunrise are predominantly of this type, which can be explained by the solar heating of the surface after sunrise inhibiting radiation fog formation. Figure 3b shows that the majority of the fog events that dissipate more than 1 hr after sunrise are followed by a low cloud base for more than 2 hr. Thus, these fog events will typically dissipate because their bases lift, without the LWP being reduced to zero. The preferred dissipation time after sunrise can be explained by the arrival of solar radiation which heats the fog and causes evaporation, an effect that will be quantified in our results.

To study the variability of temperature stratification and relative humidity above the fog, we use radiosonde measurements of these variables, and cloud radar to determine the cloud-top height (CTH) of the fog. Figure 4 is derived using 47 radiosondes at Trappes with simultaneous cloud radar measurements at SIRTA. In addition to radiosondes launched during fog, we have also included situations with very low cloud base shortly before or after a fog event. The stratification $d\theta$ (Figure 4a) shows important variability from case to case. A value of 4–8 K is the most common, but there are also cases where $d\theta$ is as low as 2 K or >10 K. The humidity of the layer above (Figure 4b) is usually above 80%, but there are also cases of humidity of 60–80% and sometimes even below 40%. The four cases of very low humidity occurred during two very persistent periods of fog and low stratus near the winter solstice when stratification was also very strong (Figure 4c).

2.3 | The case-study: A fog event on 02 November 2015

We chose a fog event which occurred at SIRTA on 02 November 2015 as a basis for the simulations (Figure 5). Fog formed nearly 2 hr before sunrise from a clear sky and quickly reached a thickness of 200 m and an LWP of 60 g/m^2. It then persisted for most of the day with horizontal visibility of around 200 m at 4 m. The elevated values of LWP makes this event a thick fog, vertically well-mixed with a profile close to adiabatic, which is confirmed by the 30 m mast measurements and the radiosonde at 1115 UTC (not shown). The radiosonde also reveals that the fog was capped by a strong inversion. The visibility gradually improved after 1200 UTC until the fog base lifted at 1440 UTC, followed by complete dissipation of the cloud by 1600 UTC. Thus, this fog is one of the more persistent events, which makes it an appropriate case to answer our research questions.

This event occurred during a synoptic situation characterized by a rather weak low-pressure system off the Atlantic coast of the Iberian Peninsula and a high-pressure system in Eastern Europe, with a southerly geostrophic wind at SIRTA. The wind direction at 10 m was easterly in the morning, turning southeasterly during the event. Integrated water vapour

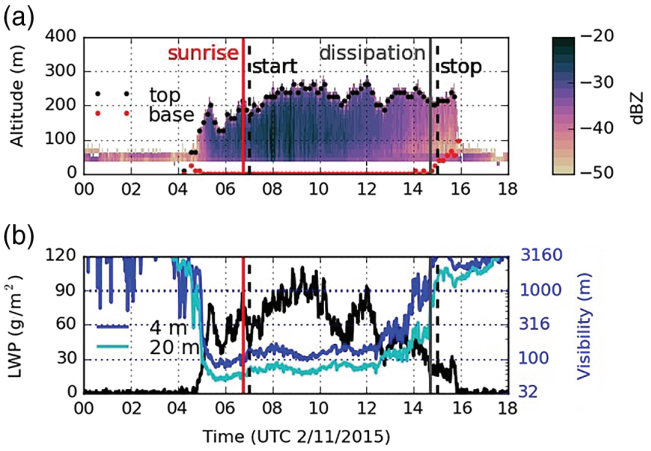

FIGURE 5 Observations from the SIRTA atmospheric observatory on 02 November 2015: (a) cloud radar reflectivity, (b) liquid water path (black) and horizontal visibility at 4 and 20 m (blue). The vertical solid lines mark the times of sunrise and fog dissipation (defined by visibility at 4 m; section 2.2). The vertical dashed lines mark the period that we simulate with the LES model (section 3.2). In (a), only the data retained after applying the noise filtering algorithm are shown, and retrievals of cloud base using ceilometer or visibility and of cloud top using the cloud radar (or visibility at 20 m) are indicated (sections 2.1 and 2.2 give details)

was around 10 kg/m^2 (observed by MWR). Important cooling occurred in the surface layer, temperature at 30 m decreasing from 16 °C the previous evening to 5 °C at 0600 UTC, 1 hr after fog formation. Measured radiative cooling of the surface was around 60 W/m^2 during most of the night, with cloud-free sky.

3 | SET-UP OF THE LARGE-EDDY SIMULATIONS

3.1 | Model description

We model the fog using the 3D Dutch Atmospheric Large-Eddy Simulation model (DALES; Heus *et al.*, 2010), version 3.2.0. An overview of the model parameter values chosen for the Baseline simulation is shown in Table 2. Certain modifications to the code were applied; these are documented in Appendix A.

The chosen model grid is a compromise between the need of a large, high-resolution domain and the limited computational resources available to us. On the one hand, LES of fog can be sensitive to the resolution, especially during the formation stage in stable stratification (Maronga and Bosveld, 2017). Since we do not model the stable formation stage (section 3.2), we avoid this challenge. The inversion layer, where the fog mixes with the layer above, is still very stable, and might require a higher model resolution than ours to properly resolve the buoyancy-generated eddies. (We estimate the Ozmidov length-scale to be in the order of 1 m in the inversion in our Baseline simulation.) On the other hand, the horizontal size of the model domain, which has cyclic lateral boundary conditions, constitutes an artificial constraint on the sizes of

TABLE 2 Values of the relevant model parameters in the Baseline run. μ_0 is the cosine of the solar zenith angle. See text for details

Parameter	Value (in Baseline)	Description
Model domain		
L_x (=L_y)	960 m	Horizontal model domain size
H	1,000 m	Vertical extent of the model domain
Δx (=Δy)	5 m	Horizontal resolution
Δz	2 m (2–30 m above 300 m)	Vertical resolution
Large-scale forcing		
V_g	5.39 m/s	Geostrophic wind speed
w_{ls}	$(-3.56 \times 10^{-6}\ s^{-1}) \times z$	Large-scale vertical velocity
Radiation model		
k	130 m^2/kg^1	Extinction coefficient of liquid water for LW radiation
F_0	75 W/m^2	Cloud-top boundary condition for LW radiation
F_1	10 W/m^2	Cloud-base boundary condition for LW radiation
SW_0	$(1187.1 - 45.9/\mu_0)$ W/m^2	Incoming direct SW radiation at cloud top
α_s	0.23	Surface albedo for SW radiation
Surface model		
LAI	2	Leaf area index
c_{veg}	0.9	Fraction of the surface covered by vegetation
C_{skin}	20 kJ m^{-2} K^{-1}	Skin layer heat capacity
Λ	5 W m^{-2} K^{-1}	Skin layer conductivity
z_{0m}	0.2 m	Roughness length for momentum
z_{0h}	0.02 m	Roughness length for heat
$W_{liq,0}$	0.2 mm	Initial surface liquid water reservoir
Microphysics		
N_c	200 cm^{-3}	Cloud droplet number concentration
σ_{gc}	1.2	Geometric standard deviation of cloud droplet size distribution
σ_{gr}	1.5	Geometric standard deviation of raindrop size distribution

the developing structures, and the model domain should therefore be sufficiently large to capture the dominating scales (de Roode *et al.*, 2004). We tested domain sizes of 450 m, 900 m and 1.8 km, and found that the dominating scale for kinetic energy was 900 m in both the 900 m and 1.8 km test runs, and that the differences between these two runs in terms of LWP and entrainment were very small (not shown). The differences were also insignificant when we compared our Baseline simulation (Table 2) to a rerun with a lower resolution of 10 m in the horizontal and 5 m in the vertical (not shown). Thus, these tests verify that our results have converged with regards to model domain size, and they give some confidence that the results are not very dependent on resolution. The height of the domain is 1 km, with a vertical resolution which decreases gradually from 2 m at 300 m to 30 m at 1 km.

Turbulence closure is ensured by the Deardorff scheme, which uses a prognostic sub-filter scale (SFS) turbulent kinetic energy (TKE) with a 3D formulation for SFS turbulent fluxes (Heus *et al.* (2010), section 2.3.1).

Advection of momentum and SFS TKE is calculated using a sixth-order centred scheme, while advection of the remaining prognostic scalars is calculated with a nearly monotonous but slightly diffusive scheme of fifth order; time integration is performed with a third-order Runge–Kutta scheme (Heus *et al.* (2010), section 2.7). Fog-top entrainment can be strongly impacted by the numerical scheme, and fifth-order schemes have been shown to be more accurate than lower-order schemes (e.g. Mazoyer *et al.*, 2017).

The interaction with the surface is parametrized using the Monin–Obukhov similarity theory coupled to a land-surface model with prognostic soil and surface skin temperature (Heus *et al.*, 2010). Canopy resistance for evapotranspiration is calculated with the Jarvis–Stewart model (Jarvis, 1976). We apply a constant value for the roughness length for momentum of 0.2 m, consistent with the friction velocity for a southeasterly wind direction at SIRTA (Fesquet *et al.*, 2009), and a ten times smaller roughness length for heat (Garratt, 1992). A typical value from literature is also chosen for the skin heat conductivity (Van Ulden and Holtslag, 1985). Leaf area index (LAI) is set to 2 and vegetation fraction to 0.9, which are close to the values used for grass and croplands in the IFS model (ECMWF, 2016), on which the DALES land-surface

model is based. The model also has a prognostic liquid water reservoir on top of the surface which can evaporate without surface resistance and is assumed to cover a fraction of the vegetation. This reservoir is fed by dew deposition, and we have also introduced that it is fed by droplet deposition (Appendix A). As this reservoir turns out to be of importance for fog dissipation, section 4.3.1 gives a further discussion.

The fog droplets are modelled with a simple one-moment scheme, using a constant prescribed number concentration N_c and a fixed log-normal shape of the size distribution with a geometric standard deviation σ_{gc}. Liquid water content (LWC) is diagnosed assuming that all water vapour exceeding the saturation threshold is liquid. From N_c, σ_{gc} and LWC, the droplet size distribution (DSD) is determined, which is then used to estimate the SW optical extinction coefficient (Appendix A) and the droplet sedimentation rate (applying Stokes' law for droplet terminal velocity). The original model did not include turbulent deposition of cloud droplets on the vegetation, but we have implemented this using the concept of a deposition velocity that provides the deposition flux when multiplied by the LWC of the first model level (Katata, 2014). We have chosen a constant deposition velocity of 2 cm/s, following e.g. Mazoyer *et al.* (2017). Drizzle drops (radius larger than 25 μm) are parametrized with the scheme of Khairoutdinov and Kogan (2000). This scheme includes autocollection, accretion, break-up, sedimentation and evaporation, and it is suitable for weakly precipitating stratocumulus clouds. The rainwater sedimentation rate is based on an empirical relationship between the drop mean volume radius and fall speed (Khairoutdinov and Kogan, 2000).

Radiative transfer is calculated with the simplified parametrizations for SW and LW radiation described in section 2.9 of Heus *et al.* (2010). These schemes only take into account the optical effect of the cloud droplets, and they therefore require boundary conditions and liquid water bulk coefficients (Table 2). The boundary conditions F_0, F_1 and SW_0 are based on comprehensive radiative transfer calculations on the fog event of 02 November 2015 using the ARTDECO (Atmospheric Radiative Transfer Database for Earth Climate Observation) code every 15 min (Wærsted *et al.* (2017) give details[1]). While the LW fluxes F_0 and F_1 are relatively constant during the fog, SW_0 depends almost linearly on the atmospheric pathway of the solar beam, which we have implemented into the model (Table 2). Following Elias *et al.* (2009), we also add an extra extinction of 0.01 m^{-1} in the SW scheme inside the fog to represent the extinction by unactivated hydrated aerosols.

The droplet concentration N_c can be an important factor for fog dissipation through its impact on the radiative processes and the droplet sedimentation; a higher N_c gives smaller droplets, which both sediment less efficiently and reflects more SW radiation due to the higher total droplet surface area (e.g. Bergot, 2013; Maalick *et al.*, 2016). However, since our model uses a one-moment microphysics scheme with prescribed droplet number concentration, this paper has limited ability to study the impacts of microphysical properties. The values of $N_c = 200\,cm^{-3}$ and $\sigma_{gc} = 1.2$ were chosen to well represent the fog interaction with SW radiation. Figure 6 shows that statistically the SW irradiance at the surface calculated with the DALES scheme agrees reasonably well with observations, when using the chosen parameter values and the observed LWP. They also agree well in our case-study (section 4.1). We are aware that deposition by sedimentation will be underestimated, since observations of the DSD at 4 m at our site indicate that N_c is often 30–100 cm^{-3} (Mazoyer, 2016), i.e. smaller than our prescribed value. The 4 m observations also usually show a wider DSD than that with $\sigma_{gc} = 1.2$, but also a bimodal shape (not shown), which we cannot represent in the log-normal model. However, the DSD in fog often varies importantly in the vertical, with higher N_c aloft than near the surface (e.g. Egli *et al.*, 2015; Price *et al.*, 2015). Since in our scheme the DSD cannot vary with altitude, we prefer to optimize the radiative behaviour rather than the agreement with observations at 4 m.

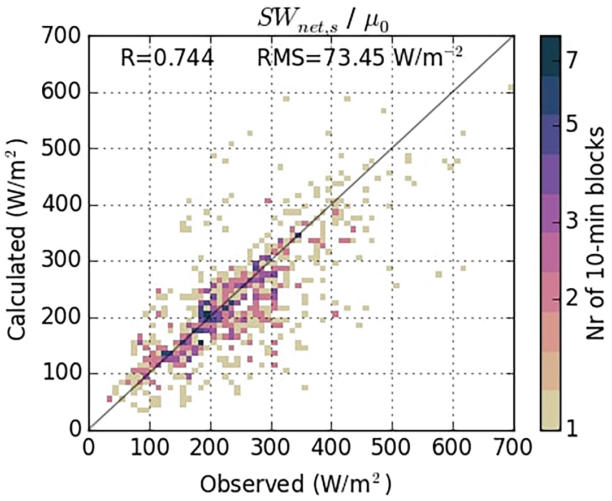

FIGURE 6 2D histogram of the mean SW irradiance absorbed at the surface, normalized with the cosine of solar zenith angle, for 10-min averaged data during 45 fog events after sunrise at SIRTA in the period 2013–2017. The (normalized) observed irradiance (by pyranometers at 10 m) is plotted against the irradiance calculated by the DALES SW scheme. This scheme uses the LWP observed by the MWR and the parameters SW_0, α_s, N_c and σ_{gc} with the values given in Table 2. The correlation (R) and root-mean-square deviation (RMS) between the observed and calculated normalised irradiances are shown

3.2 | Set-up of the sensitivity studies

Since our objective is to investigate fog dissipation after sunrise, all simulations start at 0700 UTC, which is right after sunrise. By initializing the model with fog already present, we avoid expensive computation of the stable conditions before fog formation, and we also ensure that the

[1]We use the same method for quantifying radiative flux profiles as in Wærsted *et al.* (2017), except that specific humidity input above fog comes from the radiosonde and not the MWR.

TABLE 3 List of the sensitivity runs performed with DALES, indicating which parameters and model input were changed relative to the Baseline run. The parameters are defined in Table 2

Run name	Parameter changes			Other modifications
Baseline				
NoDew	$W_{liq,0} = 0$ mm			
WeakStrat	$F_0 = 85$ W/m^2			Initial temperature and humidity profile (Figure 7)
DryAbove	$F_0 = 95$ W/m^2	and	$SW_0 = (1217.1 - 45.9/\mu_0)$ W/m^2	Initial humidity profile (Figure 7)
NoWind				No initial or forcing horizontal wind

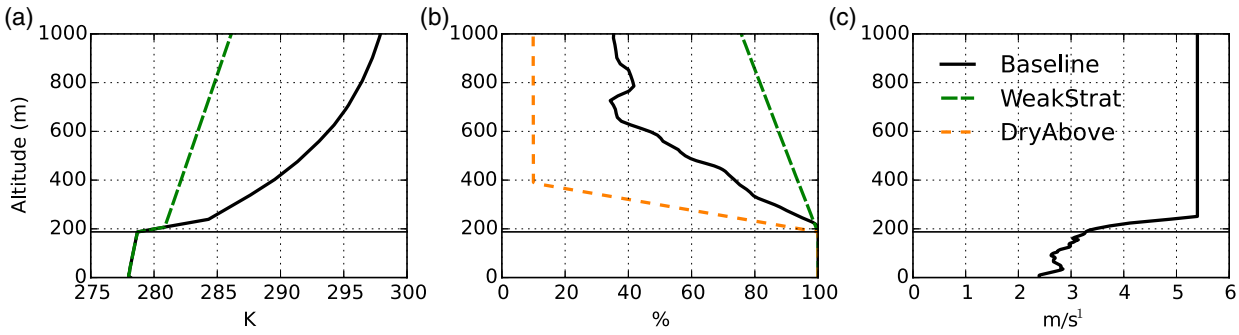

FIGURE 7 Initial profiles of (a) potential temperature, (b) relative humidity and (c) wind speed in DALES in the Baseline run, and the modified profiles in the sensitivity runs. Altitude is in metres above ground level, and the horizontal line indicates the fog top [Colour figure can be viewed at wileyonlinelibrary.com]

fog has the same starting point at sunrise in all our simulations, which makes sensitivity studies more conclusive. The model is then run until 1500 UTC with output written every 5 min for horizontally averaged profiles and every 1 min for surface quantities and mean cloud base and top. The reference simulation, called Baseline, is initialized and forced according to observations (described later in this subsection), and sensitivity studies are thereafter performed by modifying certain model inputs (Table 3 and Figure 7). In particular, we modified the initial profiles of temperature and humidity to investigate the impact of the observed variability in stratification and humidity of the layer above fog top. The Baseline simulation corresponds to a case with stable but relatively humid air above, while the run WeakStrat corresponds to the many cases with high humidity and weak stratification, and the run DryAbove represents the less common cases of dry atmosphere above fog and strong stratification (Figure 4). The imposed radiative impacts of the temperature and humidity modifications in WeakStrat and DryAbove (Table 3) are based on sensitivity calculations with ARTDECO at 1100 UTC indicating that F_0 should be increased by 10 W/m^2 in WeakStrat and by 20 W/m^2 in DryAbove relative to Baseline, and SW_0 increased by 30 W/m^2 in DryAbove, due to the different temperature and humidity profiles.

A simulation NoDew without any initial liquid at the surface is also carried out, to study the effect of this liquid reservoir. In all the other runs, the initial value for the reservoir is set to 0.2 mm, which is assumed to originate from dewfall during the night before fog forms, as no precipitation occurred. This seems a reasonable magnitude of dew based on the dew climatology from a grassland in the Netherlands, which found that average annual dewfall was 37 mm over 250 nights with dew (Jacobs *et al.*, 2006). A simulation NoWind without wind forcing is also performed, in order to test the impact of wind shear on the entrainment.

The rest of this subsection describes how the observations are used to initialize and force the Baseline run. The initial profiles use 2 hr averaged measurements (0600–0800 UTC) to get a more representative sample of the fog, as short-term variability is likely related to horizontal heterogeneity being advected past the observatory. The initial cloud top is set to the 2 hr average value of 187.5 m. Averaged radar reflectivity (Z) is used to retrieve the LWC profile with the empirical formula of Fox and Illingworth (1997):

$$LWC = 9.27 \times 10^{0.0641\,Z}, \tag{1}$$

with LWC in g/m^3 and Z in dBZ. In the cloud radar blind-zone (below ≈50 m) the LWC is assumed to increase linearly with height from 0 g/m^3 at ground level. This profile of LWC is then normalized using the LWP of the MWR, since the latter is a more reliable measurement of the integrated liquid content than the reflectivity. Initial potential temperature, humidity and wind profiles are shown in Figure 7. The temperature profile above the fog is taken from the MWR retrieval. Inside the fog it is derived from *in situ* measurements at 30 m, assuming a saturated adiabatic profile inside the fog, capped by a 0.1 K/m inversion which is imposed until it encounters the temperature profile of the MWR. Relative humidity is set to 100% inside the fog, and using the relative humidity measurements from the radiosonde launched at 1115 UTC. The initial wind profile is taken from sonic anemometers at 10 and 30 m, from the sodar in the range 30–200 m, then approaching linearly the geostrophic wind, which is used above 250 m. The geostrophic wind is constant with time and height and is taken from ERA5, the new global reanalysis of the ECMWF (Haiden *et al.*, 2017), averaging over the levels

1000, 975, 950 and 925 hPa, the times 0600 and 1200 UTC and a 2° × 2° domain around SIRTA. A time-independent large-scale subsidence is also imposed, which increases linearly by 0.356 mm/s per 100 m, starting from 0 mm/s at the surface. This vertical gradient of subsidence is determined from the average subsidence of ERA5 at 950 hPa over the times 0600 and 1200 UTC in a 2°×2° domain around SIRTA. No horizontal advection is imposed. Initial soil temperature and moisture are interpolated from SIRTA soil measurements, giving an upper soil temperature of 9 °C, and a soil moisture of 0.39 m^3/m^3. This soil moisture exceeds the field capacity parameter of the model, which means that modelled transpiration is not restricted by soil moisture.

3.3 | Analysis of the fog LWP budget

This section describes a method to separate the modelled LWP tendency into contributions from each process. This method is useful for comparing the importance of each process for the fog LWP budget, and for quantifying how much the impact from each process changes due to the modifications applied in the sensitivity tests. The idea builds on the assumption of a horizontally homogeneous well-mixed layer, which has already been used to derive budget equations for LWP in previous studies of stratocumulus layers (e.g. Van der Dussen *et al.*, 2014). In our analysis, the mixed layer is assumed to be saturated everywhere and to have a thickness h (from mean CBH to mean CTH), neglecting the horizontal variability of CBH and CTH in the model output. The saturated layer may further be well-mixed with a sub-cloud layer (after fog dissipation).

For simplicity, we neglect all horizontal variability and assume that the temperature, pressure and air density inside the fog layer can be approximated by their vertically averaged values: T_a, p, ρ_a. Actually, the temperature decreases with height in the fog layer along the saturated adiabatic lapse rate Γ_s (about −0.5 K per 100 m). The application of the vertically averaged temperature T_a in the equations below still does not introduce important errors, since the nonlinear temperature dependency of the thermodynamic quantities (e_s, de_s/dT, Γ_s) are not very large for our temperature variations of only ≈2 K in the vertical. Pressure also decreases approximately linearly with height, since the fog is much thinner than the atmospheric scale height for pressure (≈8 km). It is therefore also acceptable to use the vertically averaged pressure and air density in the equations below. Furthermore, since the temperature profile must remain saturated adiabatic, the temperature tendency will be nearly identical at all levels. Vertical mixing ensures that vertically inhomogeneous heating and cooling will be evenly redistributed throughout the layer.

Since the air is assumed to be at saturation, the water vapour pressure e_a must equal its saturation value e_s at the fog temperature, i.e. $e_a = e_s(T_a)$. If T_a increases (decreases), the vapour pressure must increase (decrease) so that the air remains saturated at the new temperature:

$$\frac{de_a}{dt} = s\frac{dT_a}{dt}, \tag{2}$$

where $s = de_s/dT$. Since the specific humidity q_v relates to vapour pressure as $q_v = (\epsilon/p)e_a$, we may rewrite Equation 2 as

$$\gamma\frac{L_v}{c_p}\frac{dq_v}{dt} = s\frac{dT_a}{dt}, \tag{3}$$

where $\gamma = c_p p/(\epsilon L_v)$ is the psychrometric constant, $\epsilon = 0.622$ is the ratio of the gas constants of dry air and water vapour, $c_p = 1{,}004\,J\,kg^{-1}\,K^{-1}$ is the specific heat capacity of air at constant pressure, and $L_v = 2.5\times10^6$ J/kg is the specific latent heat of vaporization. We have neglected the insignificant contribution from the rate of change of pressure to the tendency of q_v.

An increase (decrease) in q_v can come from evaporation (condensation) of the liquid water on the fog droplets, which constitutes a sink (source) of fog LWP. The integrated evaporation rate of droplets is denoted E_a, with SI units of $kg\,m^{-2}\,s^{-1}$, more conveniently given in $g\,m^{-2}\,hr^{-1}$ later in the paper. q_v is also affected by latent heat fluxes (i.e. water vapour fluxes) at CBH and CTH. Thus:

$$\frac{dq_v}{dt} = \frac{1}{\rho_a h}\left\{E_a + \frac{1}{L_v}(LH_{base} + LH_{top})\right\}, \tag{4}$$

where LH_{base} and LH_{top} have units of W/m^2 and are defined positive when they bring moisture into the cloud.

The fog is also subjected to sensible heating, which we define positive when it brings heat into the fog cloud. The total sensible heat flux (in W/m^2) is a sum of contributions from five processes: net absorbed LW radiation (SH_{LW}), net absorbed SW radiation (SH_{SW}), adiabatic heating due to subsidence (SH_{sub}), and turbulent sensible heat fluxes at cloud base (SH_{base}) and cloud top (SH_{top}):

$$SH_{tot} = SH_{LW} + SH_{SW} + SH_{sub} + SH_{base} + SH_{top}\,. \tag{5}$$

T_a is increased by the sensible heat fluxes, while it is decreased by the latent heat of evaporation of the droplets:

$$\frac{dT_a}{dt} = \frac{1}{\rho_a c_p h}\left(-L_v E_a + SH_{tot}\right). \tag{6}$$

By inserting Equations 4, 6 into Equation 3, we can eliminate dT_a/dt and dq_v/dt:

$$\gamma\frac{L_v}{c_p}\frac{1}{\rho_a h}\left\{E_a + \frac{1}{L_v}\left(LH_{base} + LH_{top}\right)\right\} = \frac{s}{\rho_a c_p h}(-L_v E_a + SH_{tot}).$$

Some rearrangement of this equation results in the following expression for E_a:

$$E_a = \frac{s}{s+\gamma}\frac{1}{L_v}SH_{tot} - \frac{\gamma}{s+\gamma}\frac{1}{L_v}\left(LH_{base} + LH_{top}\right). \tag{7}$$

Since Equation 7 is a linear sum over the fluxes from different processes, the contributions to E_a of each process are additive and can be analysed separately. While positive sensible heat fluxes cause loss of liquid water (positive contribution to E_a), positive latent heat fluxes provide a gain of liquid water (negative contribution to E_a). Because s increases

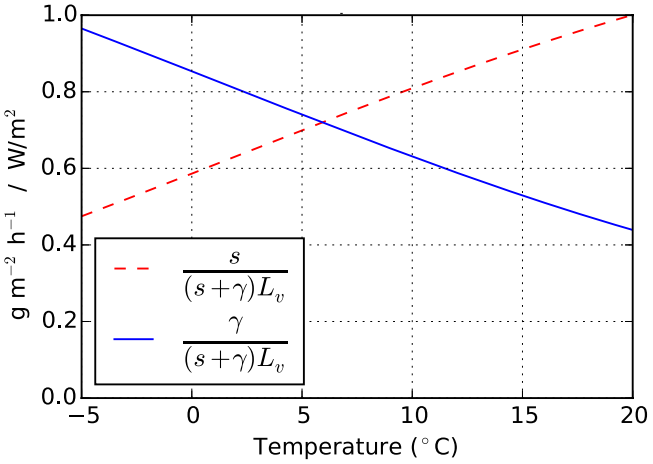

FIGURE 8 The fog evaporation rate (g m^{-2} hr^{-1}; dashed line) caused by a sensible heat flux of 1 W/m^2, and the condensation rate (solid line) caused by a latent heat flux of 1 W/m^2, as a function of temperature at a pressure of 1,000 hPa. They are the coefficients in Equation 7 [Colour figure can be viewed at wileyonlinelibrary.com]

TABLE 4 Separation of Equation 8 onto the terms shown in Figure 10

Process	Contribution to Equation 8
LW cooling	$-\frac{s}{s+\gamma}\frac{1}{L_v}SH_{\mathrm{LW}}$
SW absorption	$-\frac{s}{s+\gamma}\frac{1}{L_v}SH_{\mathrm{SW}}$
Turbulent sensible heat (base)	$-\frac{s}{s+\gamma}\frac{1}{L_v}SH_{\mathrm{base}}$
Turbulent latent heat (base)	$\frac{\gamma}{s+\gamma}\frac{1}{L_v}LH_{\mathrm{base}}$
Sedimentation (base)	$F_{\mathrm{liq,base,Sed}}$ (Equation B7)
Turbulent liquid flux (base)	$F_{\mathrm{liq,base,Turb}}$ (Equation B8)
Subsidence	$-\frac{s}{s+\gamma}\frac{1}{L_v}SH_{\mathrm{sub}}+\frac{\mathrm{d}w_{\mathrm{ls}}}{\mathrm{d}z}LWP$
Entrainment	$-\frac{s}{s+\gamma}\frac{1}{L_v}SH_{\mathrm{top}}+\frac{\gamma}{s+\gamma}\frac{1}{L_v}LH_{\mathrm{top}}+F_{\mathrm{liq,top}}$

with temperature, the effects of sensible heat fluxes become increasingly important with temperature, while the opposite is the case for latent heat fluxes (Figure 8).

To get the full fog LWP budget, we need to take into account also the vertical fluxes of liquid water across the fog base and top, which have contributions from turbulent mixing and sedimentation of droplets (Appendix B). We call these liquid fluxes $F_{\mathrm{liq,base}}$ and $F_{\mathrm{liq,top}}$, defined positive when liquid is transported towards the fog. Finally, we account for the reduction in LWP caused by the horizontal divergence due to the vertical gradient of subsidence ($\mathrm{d}w_{\mathrm{ls}}/\mathrm{d}z = -3.56\times10^{-6}\,\mathrm{s}^{-1}$; Table 2). The final expression for the fog LWP tendency is then:

$$\frac{\mathrm{d}LWP}{\mathrm{d}t} = -E_{\mathrm{a}} + F_{\mathrm{liq,base}} + F_{\mathrm{liq,top}} + \frac{\mathrm{d}w_{\mathrm{ls}}}{\mathrm{d}z}LWP. \qquad (8)$$

Table 4 indicates which terms in Equation 8 are attributed to each process in our analysis. Appendix B gives more details on how each of the SH, LH and F_{liq} terms are calculated from the model output. Note in particular that the fluxes at fog base and top also include the impact of model levels added to or removed from the cloud layer when CBH and CTH change with time.

4 | RESULTS AND DISCUSSIONS

4.1 | Comparison of the Baseline simulation to observations

Figure 9 shows the evolution of the fog in the Baseline simulation compared to the observed fog. We note that the modelled fog base lifts several hours earlier than the observed fog base, dissipating at the surface at 1045 UTC, although the LWP is higher. The earlier lifting may be related to the vertical development of the mixed layer being stronger in the model than observed, thereby lifting the liquid layer up from the surface. However, the temperature evolves similarly to observations. The relative similarity between model and observations indicates that the local processes likely played an important role in the evolution of the fog, although we cannot exclude that advection and other large-scale phenomena also played a role in the observed fog.

We now consider the energy budget of the surface (Figure 9d). The net radiation (R_{net}) is mainly driven by the SW and therefore evolves with the solar angle, reaching a maximum around noon. However, the dependence on LWP is also apparent, especially in the anti-correlated relationship between the observed R_{net} and the observed LWP (Figure 9b). The rather good agreement between observed and modelled R_{net} can thus be explained by the similar evolutions of LWP, which is the main parameter affecting how much radiation reaches the surface (Wærsted *et al.*, 2017). The ground flux (G) is upward in this case, due to the soil being warmer than the air, and its contribution is in the order of 10–15 W/m^2 in the morning both in model and observations.

We now turn to the surface sensible heat flux (SH) and latent heat flux (LE). Here the model and observations are no longer similar. The model predicts a Bowen ratio of around 2 after 1000 UTC, and considerably higher in the early morning because of higher surface resistance due to low insolation (section 4.3.1), but the LE contribution to surface energy balance is nevertheless significant. The observations show a considerably lower SH and an LE around zero. As a result, on average only 35% of the available energy ($R_{\mathrm{net}} - G$) is accounted for by the turbulent heat fluxes. The lack of closure in the surface energy balance indicates that the turbulent flux observations must be better understood before they can be used to validate the predicted repartition of the available energy into SH and LE in the model. The challenge of the surface energy balance is discussed further in section 4.3.1.

4.2 | Impacts of physical processes on fog LWP

Figure 10 separates the modelled tendency of fog LWP into contributions from each physical process, as explained in section 3.3. We first note that the LWP budget closes well: the residual is small compared to the important terms and it is centred at zero, except for the first half hour. This indicates that the method of decomposition of the LWP budget in the model works well in spite of the simplifications applied.

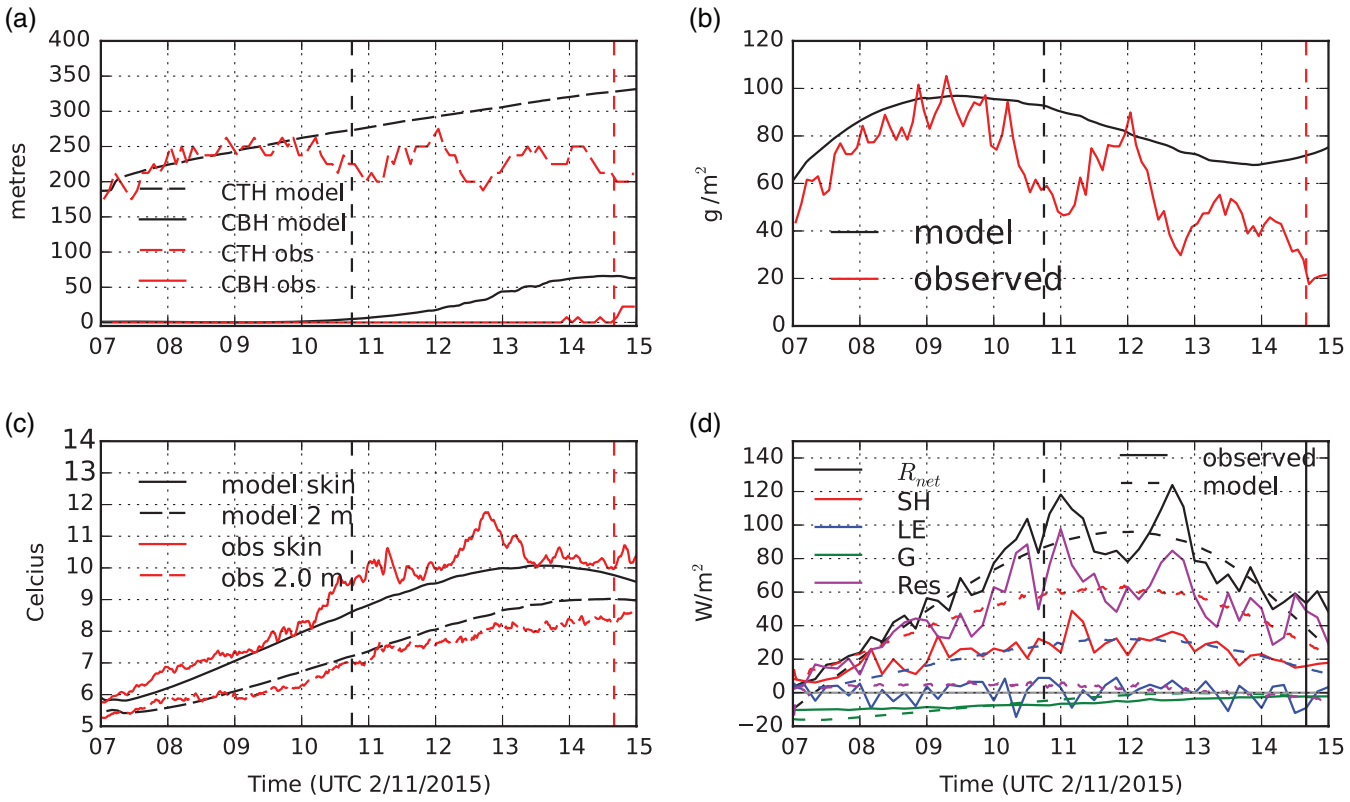

FIGURE 9 Evolution of the fog in the Baseline simulation (black lines) and observations (5 min averages, red lines) of the real fog on 02 November 2015. (a) Heights of cloud top and cloud base, (b) LWP (the model includes both cloud water and rainwater), (c) screen and surface skin temperature. (d) shows terms in the surface energy budget, in the Baseline simulation (solid) and observations (10 min averages, dashed): net radiation absorbed (R_{net}), upward sensible (SH) and latent (LE) turbulent heat fluxes, and downward ground flux (G). The residual (Res) is calculated as $R_{\text{net}} - G - SH - LE$. The vertical dashed lines indicate the time of dissipation. In the observations, it is defined from the visibility at 4 m (section 2.2). In the model, dissipation is defined as the first time when average CBH is above 4 m

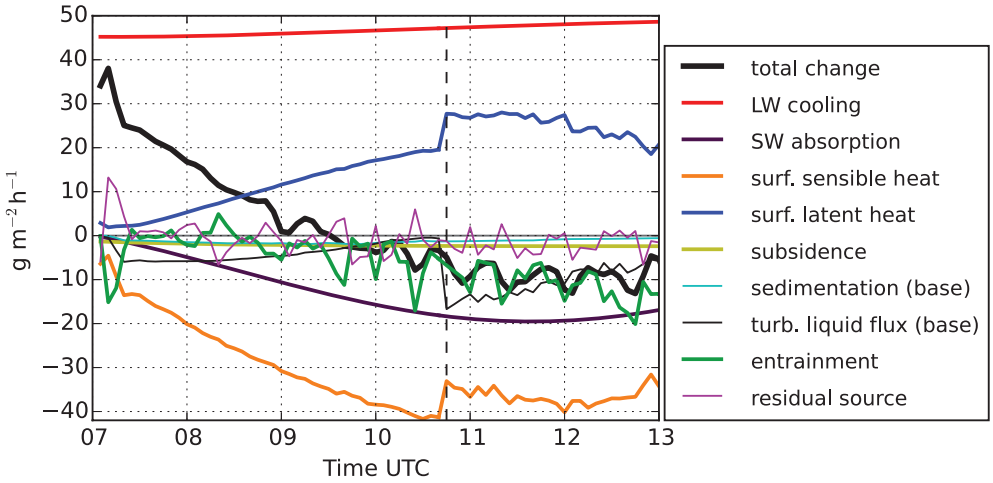

FIGURE 10 The terms of the fog LWP budget in the Baseline simulation, calculated from the model output (Equations 7, 8 and Appendix B). The bold black line denotes the change with time of fog LWP in the model, while the other lines are the contributions from each process (Note that the lines for sedimentation and subsidence are almost superimposed near −2). The pink line is the residual, i.e. the total change in LWP minus the sum of all contributions. The vertical dashed line marks the time of dissipation in the model (as in Figure 9)

We further note that the residual is strikingly anti-correlated with the entrainment term, indicating that the residual mainly can be attributed to this term, as discussed in Appendix B. We have therefore chosen in the later figures to derive the entrainment term from the residual of the other terms of the LWP budget.

The LWP increases until 0930 UTC, after which it decreases, but only by 5–10 g m^{-2} hr^{-1}. The increase in the early morning is due to the LW radiative cooling. In comparison, heating and divergence by subsidence play a negligible role due to the weak large-scale velocity. As the sun rises, the absorption of solar radiation inside the

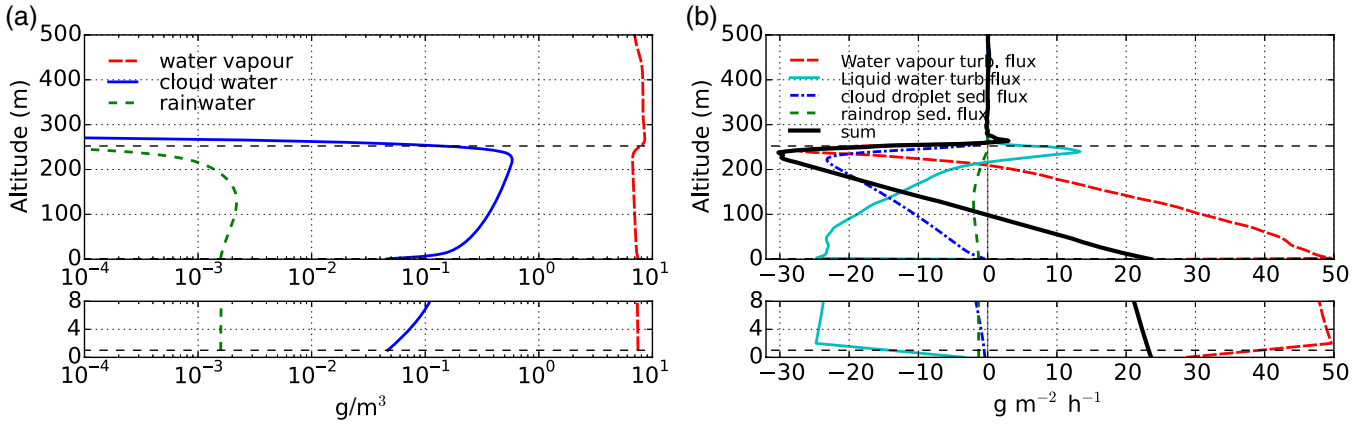

FIGURE 11 Horizontally averaged profiles at 0930 UTC in the Baseline simulation: (a) water vapour, cloud water and rainwater content, and (b) upward fluxes of water (by turbulence and sedimentation). The horizontal dashed lines indicate the cloud base and cloud top. The lower panels are just enlargements of the lowest parts of the profiles [Colour figure can be viewed at wileyonlinelibrary.com]

fog layer becomes an increasingly important loss term of LWP; its magnitude is in agreement with what we calculated in Wærsted *et al.* (2017) if the absorption by unactivated aerosols of optical depth 0.05 is accounted for.

The most significant negative term in the LWP budget is the sensible heat flux from the surface, which increases rapidly as the sun rises. However, the contribution from surface latent heat flux is also important and has the opposite sign. At our fog temperature of 5–8 °C, each 1 W/m^2 of latent heat gives approximately the same LWP to the fog as is lost by 1 W/m^2 of sensible heat (Figure 8), making their combined effect roughly proportional to $SH - LE$. The Bowen ratio is therefore very important for the combined effect of the surface heat fluxes on the fog LWP.

The droplet sedimentation rate at the surface is very weak, because the LWC is low near the surface (Figure 11a), while sedimentation contributes importantly to vertical transport of water within the fog (Figure 11b). The low LWC near the ground also limits the amount of turbulent deposition, which is still a stronger contributor than sedimentation (Figure 10). Our results are not very sensitive to this added deposition; in a test run where the turbulent liquid deposition was not included, the fog LWP was 5% higher than in Baseline at 1000 UTC, and dissipation was 15 min later (not shown). This is a weaker impact on LWP than we would expect from removing the term "turb. liquid flux (base)" in Figure 10. There is actually a compensating effect through a higher Bowen ratio caused by a smaller surface liquid reservoir, due to less feeding by deposition.

The weak deposition can likely be explained by the heating from the surface. Since the surface sensible heat flux is larger than the latent heat flux, the turbulent exchange between the surface and the first model level tends to make the air subsaturated. To preserve saturation, fog droplets need to evaporate in the first model level. Figure 11b shows that at the first model level, there is a strong convergence of liquid water (downward liquid flux is $\approx$20 g m^{-2} hr^{-1} higher at 2 m than at 0 m) and a corresponding divergence of water vapour (upward vapour flux is $\approx$20 g m^{-2} hr^{-1} higher at 2 m than at 0 m). Thus, there is an evaporation of $\approx$20 g m^{-2} hr^{-1} at the first model level, which explains its low content of cloud water (Figure 11a). This sharp flux shift at the first model level is also the reason for the sudden change in the LWP budget terms when the fog base lifts (Appendix B). Thus, deposition is weak because the LWC near the surface is kept low by the surface heating.

The drizzle parametrization generates little rainwater (it is highest around 0930 UTC), but contrary to the cloud water the raindrops do not evaporate as efficiently near the surface, and they produce a sedimentation flux at the surface which is twice as large as that of cloud droplets, although both are in the order of 1 g m^{-2} hr^{-1} only (Figure 11b). However, the cloud droplet sedimentation is sensitive to the chosen parameters for the DSD, and we likely underestimate it to some extent (section 3.1).

Entrainment at fog top is only a weak sink of LWP in the Baseline run. It amounts to less than 10 g m^{-2} hr^{-1} in the first hours of the simulation (Figure 10). This is because the layer directly above the fog is saturated in the initial conditions (Figure 7). As the fog develops vertically, it comes into contact with layers of lower relative humidity, so that the loss from entrainment increases with time. In addition to being a sink of LWP, the entrainment also acts to increase the thickness of the mixed layer. Since clouds always stick to the top of a mixed layer (because the layer is coldest at the top), the fog base will lift from the ground if the layer becomes sufficiently thick. The faster increase of the cloud-top height in the model than in the observations (Figure 9) can therefore have contributed to the earlier lifting of the cloud base in the model. The role of entrainment will be further explored in section 4.3.2.

All in all, the LWP budget of the Baseline simulation suggests that, once the sun has risen significally, the radiative heating of the surface is the main loss process for fog LWP, with a strong importance of the Bowen ratio, followed by the SW absorption inside the fog.

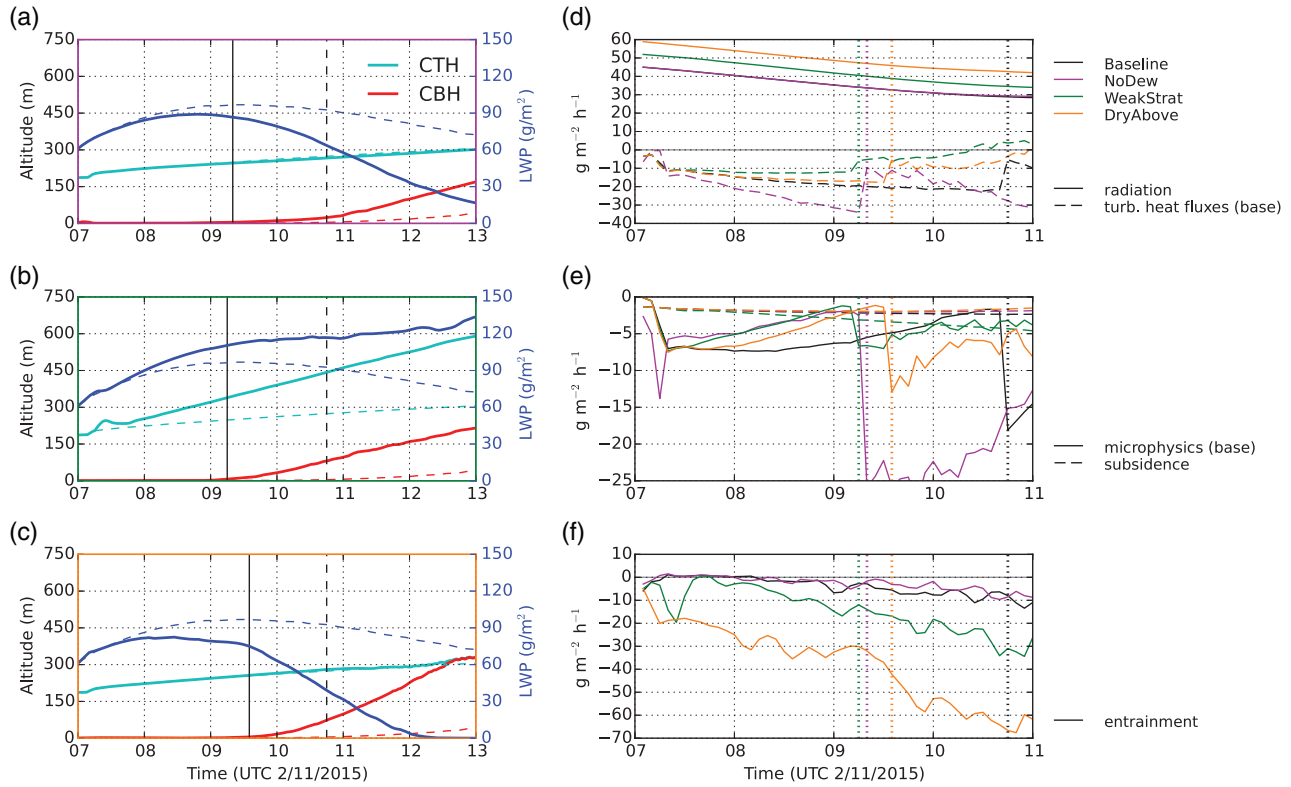

FIGURE 12 (a–c) Comparison of the modelled fog base (red), fog top (cyan), LWP (blue), and dissipation time (as defined in Figure 9, vertical lines), between Baseline (dashed) and each of the sensitivity runs (solid): (a) NoDew, (b) WeakStrat, and (c) DryAbove. (d–f) Comparison of the terms in the LWP budget equation for the four runs. "Radiation" includes both SW and LW, "turb. heat fluxes (base)" is the combined effect of turbulent sensible and latent heat at CBH, and "microphysics" combines sedimentation and turbulent liquid flux at CBH (i.e. all liquid transport across CBH). There is no residual because the entrainment term has been derived from LWP closure rather than calculated. The dissipation times in each of the four runs are marked as vertical, dotted lines. NB: In (d), the lines "radiation" of Baseline and NoDew are superimposed

4.3 | Sensitivity studies

4.3.1 | A wet surface and the surface energy balance

In the NoDew run, the LWP is depleted sooner and more rapidly, leading to an 85 min earlier dissipation by lifting of the cloud base, while the cloud top develops very similarly to Baseline (Figure 12a). Consequently, the cloud base lifts sooner. Clearly it is the larger loss by surface fluxes ($10\,\mathrm{g\,m^{-2}\,hr^{-1}}$ more over 0800–0915 UTC, Figure 12d) that is responsible for the faster decrease in LWP in NoDew than Baseline. The impacts on LWP by radiation and entrainment are the same as Baseline (Figure 12d,f), while the loss by deposition is smaller before dissipation ("microphysics", Figure 12e), due to the earlier reduction in liquid near the ground. After dissipation, the microphysics term becomes very big, but this is actually representing the mixing of the droplets with the unsaturated air from the sub-cloud layer, compensating the decrease in the "turb. heat fluxes (base)" term at dissipation (i.e. it is a consequence of our definition of the terms; section 4.2). The increased loss from surface turbulent heat fluxes relative to Baseline is due to a higher Bowen ratio, caused by the extra surface resistance involved when evaporation cannot occur directly from the surface.

Thus, this sensitivity test indicates that the presence of a liquid layer on top of the surface can importantly affect the dissipation of fog. Although the soil is very moist, the relatively low temperature and small amount of solar radiation makes the canopy resistance very high compared to the aerodynamic resistance, especially in the first hours after sunrise (Figure 13a). This means that the evaporation through transpiration will be low, in spite of the high soil moisture. For the fraction of vegetation covered by liquid, however, there is no surface resistance, and we can therefore expect a Bowen ratio of γ/s from the Penman equation (Penman, 1948), so that the surface fluxes cause no evaporation of the fog. (To see this, insert $SH_{\mathrm{base}} = (\gamma/s)LH_{\mathrm{base}}$ in Table 4, which results in exactly opposite impacts on LWP of SH_{base} and LH_{base}). It is the difference in the fraction of vegetation covered by liquid (c_{liq}) that causes a higher overall Bowen ratio in NoDew relative to Baseline (Figure 13d). This fraction is very low in NoDew, while in Baseline it starts at 0.5 and then decreases (Figure 13c). In DALES, this fraction is parametrized rather crudely as being proportional to the surface liquid water reservoir W_{liq}:

$$c_{\mathrm{liq}} = \frac{W_{liq}}{0.2\mathrm{mm} \times LAI}. \tag{9}$$

Since $LAI = 2$ and the initial liquid water reservoir in Baseline is 0.2 mm (Table 2), the fraction c_{liq} is 0.5 initially, and then it decreases due to evaporation. Although Equation 9 is probably too simple for real situations, the sensitivity test has

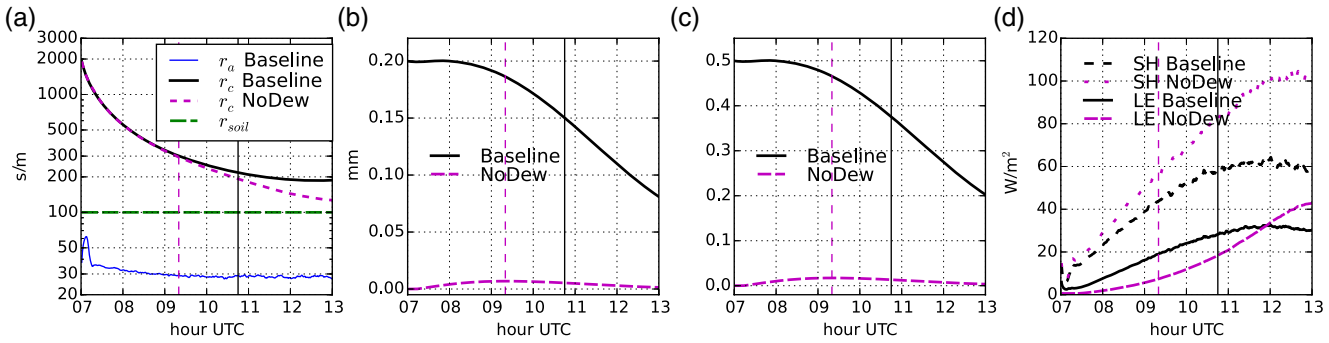

FIGURE 13 Simulated variables in the surface parametrization in DALES for the runs Baseline and NoDew, as a function of time: (a) aerodynamic resistance (r_a), canopy resistance (r_c, applied to the fraction of vegetation not covered by liquid) and soil resistance (r_{soil}, a prescribed value applied to the 10% of the surface assumed not to have vegetation); (b) surface liquid water reservoir (W_{liq}); (c) fraction of vegetation covered by the liquid (c_{liq}); and (d) surface sensible and latent heat fluxes. Vertical lines indicate the dissipation times in Baseline (solid) and NoDew (dashed). In (a), r_a in NoDew is not shown because it is always very close to that of Baseline [Colour figure can be viewed at wileyonlinelibrary.com]

shown the importance of a wet surface for maintaining fog after sunrise. Since the evaporation occurs at microscale, it is to be expected that the fraction of the surface covered by liquid is more important for the Bowen ratio than the total liquid reservoir. In reality, the vegetation type can be expected to strongly impact how much of the surface stays wet as the water is redistributed by wind, throughfall, and infiltration to the soil. The fog itself could help maintain a high liquid coverage due to deposition of cloud droplets on the vegetation. Price (1991) studied the evaporation over a bog and found it to be close to equilibrium evaporation during fog, arguing that this was enabled by fog drip which wetted the surface. Wetting of the surface could also be caused by rainfall before or during the fog.

Given the importance of the Bowen ratio for the fog LWP budget, validation of model predictions is important. The two main uncertainty sources for the simulated Bowen ratio are likely (a) the estimation of the fractional liquid cover of the surface, and (b) the possible deviations of plant behaviour from the Jarvis–Stewart model during fog, since the model was derived for daytime convective conditions originally. Unfortunately, since the closure in the observed energy balance is only 35% (Figure 9d), it leaves too much uncertainty to perform such a validation. However, the low closure percentage not only occurs in fog. We considered the whole month of November 2015, and found that during day (for solar zenith angle less than 85°), the average closure is 43%. This is a worse closure than reported for the autumn daytime in the Ebro Valley by Cuxart *et al.* (2015) (they found that the residual was 34% of R_{net}). The non-closure of the surface energy balance is a well-known issue in micrometeorology, and it is common that the available energy ($R_{net} - G$) is larger than the measured turbulent heat fluxes ($SH + LE$) (Foken, 2008). This positive residual is likely explained either by a non-negligible storage term in the uppermost soil and vegetation or an underestimation of the turbulent fluxes, since R_{net} is rather precisely measured (Leuning *et al.*, 2012). In our case the residual is too large to be mainly explained by storage, and it seems more likely that an underestimation of the turbulent heat fluxes is the main reason for the non-closure. Foken (2008) argues that this underestimation occurs not merely due to measurement errors, but also because of coherent mesoscale circulations, generated by surface heterogeneities, whose flux contributions cannot be detected by covariances at a single location. Evidence for this theory has been found from the improved closure obtained from scintillometers (which are able to measure averaged fluxes over a larger area), and from the good closure obtained in very homogeneous landscapes such as deserts (Foken, 2008). SIRTA lies in a heterogeneous landscape, which may contribute to the poor closure. However, we found a similarly low closure (46%) for the observatory at Cabauw in the Netherlands (Beljaars and Bosveld, 1997) for daytime in November 2011, which was a similar period to November 2015 at SIRTA (including several fog events and with R_{net} rarely higher than 200 W/m^2).

Although surface energy balance measurements are a topic of much research, to our knowledge no publication has studied it specifically for fog. Our results show that it is worth investigating. Alternative measurement techniques such as scintillometers could be utilized to see if they measure the turbulent fluxes in fog better than the eddy covariance method.

4.3.2 | The stratification and humidity above the fog

In WeakStrat, the cloud top develops much faster than in Baseline (Figure 12b). Due to the weaker stratification, less potential energy needs to be overcome to mix the fog with the air above, and therefore the entrainment can happen much faster. The entrainment velocity, defined as the rate at which the fog top penetrates into the layer above, is calculated as the change in CTH with time minus the subsidence velocity at CTH. The average entrainment velocity in the period 0800–1000 UTC amounts to 72.7 m/hr in WeakStrat, compared to 22.2 m/hr in Baseline. This vertical displacement of the fog top enables a dissipation of the fog at ground level 90 min earlier than in Baseline. The earlier dissipation occurs in spite of a higher LWP. This sensitivity

test therefore shows that the dissipation of fog at ground level (i.e. lifting of the cloud base) can depend as much on the evolution of the CTH as the LWP. The LWP increases more in WeakStrat than in Baseline in spite of the larger loss by entrainment (Figure 12f). This can be explained by the stronger radiative cooling, and by the weaker loss by turbulent heat fluxes at cloud base (eventually even becoming a gain) once there is a sub-cloud layer (Figure 12d). There is also less loss by deposition in WeakStrat than Baseline (the term "microphysics" in Figure 12e); this is because the LWC near the surface decreases more rapidly due to the upward displacement of the liquid water associated with the thickening of the mixed layer.

In the DryAbove run, the fog more rapidly loses liquid water and lifts 70 min earlier than in Baseline, and the whole cloud dissipates around noon (Figure 12c). Even though there is not more entrainment than in Baseline (cloud top develops at the same rate), the introduced air is much drier and therefore causes much more liquid water loss (Figure 12f). However, the dry air above the fog also has an opposite effect: due to less water vapour in the atmospheric column, the greenhouse effect is weaker so that the radiative cooling of the fog top is stronger than in Baseline (as calculated in section 3.2), leading to a stronger production of LWP by LW cooling (Figure 12d). This second effect amounts to an additional 13 $g\,m^{-2}\,hr^{-1}$ of LWP production. It is still smaller than the increased LWP loss through entrainment, which amounts to 33 $g\,m^{-2}\,hr^{-1}$ on average in the period 0800–1000 UTC. All in all, the LWP budget is therefore more negative than in Baseline, leading to stronger LWP decrease. Thus, similarly to NoDew, in the DryAbove run the fog dissipates earlier than in Baseline because the LWP is smaller with the same fog thickness.

An overall interpretation of the three sensitivity tests is that the fog dissipation at the surface occurs when the fog LWP is no longer sufficient to fill the entire mixed layer, so that the fog base lifts. Dissipation can be triggered from a decrease in LWP or an increase in the CTH. In NoDew and DryAbove, it is the decrease in LWP that explains the earlier dissipation, while for WeakStrat it is the increase in CTH.

The difference in fog-top stratification between the runs Baseline and WeakStrat, which causes a large difference in entrainment velocity (Figure 12b), represents the span of observed stratification at fog top (Figure 4c). This indicates that fog-top stratification is a major factor controlling fog dissipation. In situations when the fog top is capped by a weaker inversion and a weak stability in the overlying hundreds of metres, it will more easily thicken and transition into stratus than in situations when the fog is capped by a stronger inversion. Observations of fog-top stratification might therefore be useful for anticipating fog dissipation. As radiosondes only give snapshots of the situation, the observation by MWR is more practical. We find that the MWR reproduces the parameter $d\theta$ observed by radiosondes (Figure 4a) with a correlation coefficient of 0.92, although it systematically underestimates $d\theta$ for strong stratification (not shown).

The entrainment velocity at the fog top not only depends on the stratification, but also on the amount of TKE available to overcome the potential energy of the stratification. Several entrainment parametrizations have been developed for the clear or stratocumulus-topped convective boundary layer. These essentially compute the entrainment velocity as a ratio of the produced TKE in the mixed layer to the stability of the capping inversion (Stevens, 2002; Conzemius and Fedorovich, 2006). TKE can be produced both by buoyancy and wind shear. In our case, the fog layer is efficiently destabilized by cooling at the top and heating from the surface, and wind shear is present at the surface and at fog top.

Figure 14a,b shows the vertical profiles of the terms in the budgets of resolved TKE and SFS TKE in the Baseline simulation, averaged in the period 0915–0945. Figure 14a shows that both wind shear and buoyancy give important contributions to the production of resolved TKE in the model after sunrise. The SFS TKE comprises less than 10% of the total TKE at all altitudes except below 20 m (not shown), and the SFS TKE budget is balanced between production and dissipation on each level above 10 m (Figure 14b). The wind shear production of resolved TKE is near the surface and in the entrainment zone (Figure 14a). However, most of the TKE produced by shear near the surface is dissipated locally, and previous studies have shown that surface shear gives a negligible contribution to entrainment (Conzemius and Fedorovich, 2006). In a sensitivity run NoWind, where wind forcing and initial wind were both set to zero, the average entrainment velocity in the period 0800–1000 UTC was 20% lower than in the Baseline set-up (not shown). The resolved TKE budget of the NoWind run (Figure 14c) shows that the lack of shear production near the fog top has been largely compensated by an increase in the transport of TKE from the lower parts of the fog to the top. Our sensitivity study therefore indicates that entrainment is not strongly reduced in the absence of wind shear, as long as there is important TKE production by buoyancy. The impact of buoyancy on entrainment suggested by e.g. Stevens (2002) makes it likely that fog thickening by entrainment is enhanced by heating of the surface, thus likely being more efficient in spring/autumn than near the winter solstice. Likewise, the entrainment could also be stronger for thick (opaque) fog than for thin fog, due to the stronger radiative cooling at fog top (Wærsted *et al.*, 2017).

As shown in the run DryAbove, the humidity above the fog also has an impact on fog dissipation and could be an interesting parameter to observe. However, its effect is less straightforward due to the opposing impacts on LWP of radiation and entrainment, which both increase when the air above is dry (Figure 12d,f). These two processes are not sensitive to the humidity at the same altitudes. While the drying effect from entrainment is only affected by the humidity in the first few tens of metres above the fog top, with which the fog mixes, the radiative impact is also sensitive to the atmosphere

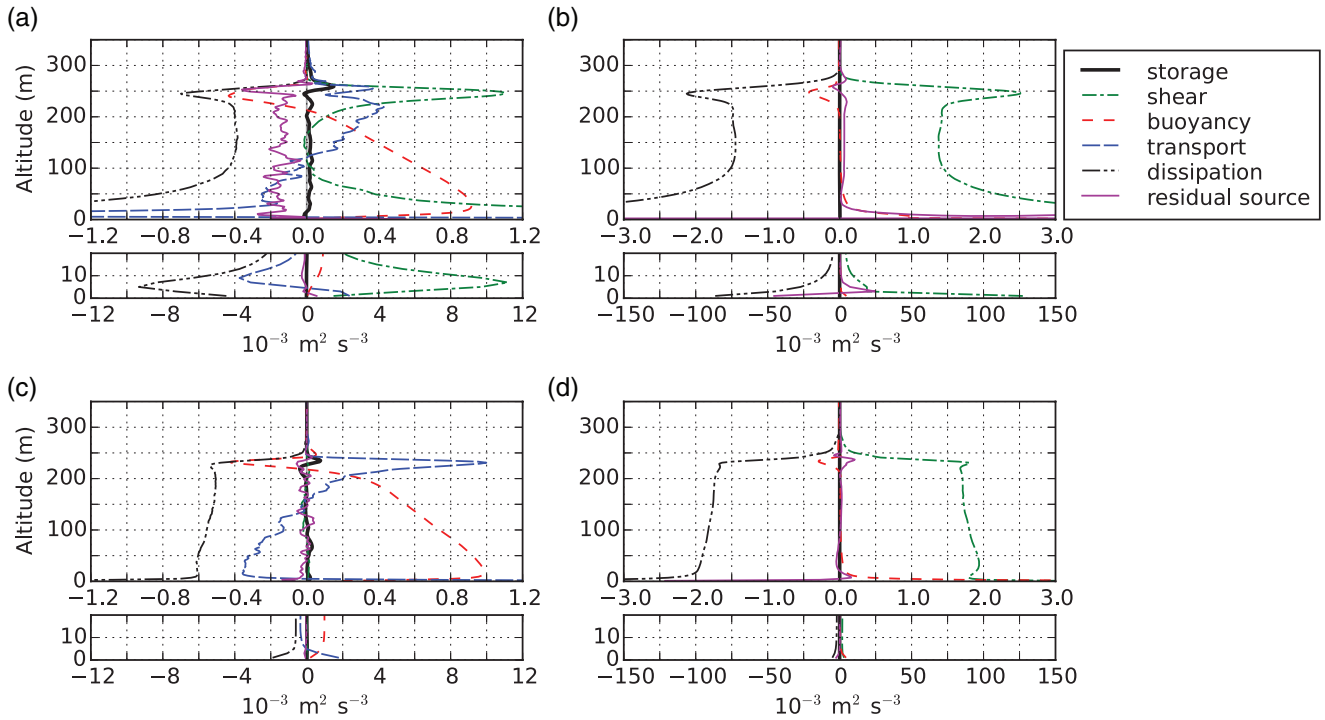

FIGURE 14 The profile of (a, c) resolved and (b, d) sub-filter-scale TKE budget, averaged over 0915–0945 UTC, in (a, b) the Baseline run and (c, d) the NoWind run. The term "storage" is the increase in TKE, while "residual source" is the storage minus the sum of the other terms (i.e. the source of TKE which is not accounted for). Each panel has a separate plot below showing the lowest 20 m at an adjusted scale

higher up. This means that in special cases where there is a humid layer directly above the fog top while the rest of the atmosphere above is very dry, the radiative effect would dominate and the fog could be more resistant to dissipation than when the atmosphere is moister. Indeed, this is likely what happened during the periods of persistent fog which correspond to the four radiosondes in Figure 4 with lowest humidity. The combination of a strong stratification and little insolation near the winter solstice limits the entrainment, so that the radiative effect of the dry atmosphere can dominate over the entrainment effect. If the humidity in the layer directly above fog top is to be observed by remote sensing (without confusing it with the fog or the humidity higher up), an instrument with both high vertical resolution and the ability to penetrate the fog is needed. The MWR humidity profile lacks the resolution, while differential absorption lidars, which would have sufficient resolution (Spuler *et al.*, 2015), cannot penetrate clouds. An alternative would be to measure the layer *in situ*, for example using a drone.

5 | SUMMARY AND CONCLUSIONS

Fog dissipation depends on processes occurring both at the surface and the fog top, and the increasing possibilities for measuring properties aloft, *in situ* or by remote sensing, make it important to understand the impacts of the fog-top properties. Using observations of 250 fog events during 7 years, we showed that more than half the fog events dissipating after sunrise transition to a stratus which lasts at least 2 hr, indicating that the vertical displacement of the liquid layer is the most frequent dissipation scenario. We further quantified the contribution of different local processes to the liquid water path (LWP) budget of a thick fog after sunrise, and investigated how the fog dissipation is affected by the temperature and humidity at the fog top, and by the liquid water at the surface. This was achieved using idealized sensitivity simulations carried out with the large-eddy model DALES, where we tested the impact of the variability of fog-top properties observed by 47 radiosondes and cloud radar.

The quantifications of the terms of the fog LWP budget in the simulations indicate that the most important loss process of LWP is the turbulent heat fluxes from the surface, responsible for 20–30 g m^{-2} hr^{-1} in the late morning (combined effect of sensible and latent heat flux). The loss by absorption of SW radiation in the fog layer reaches 15 g m^{-2} hr^{-1} in the late morning. The loss by cloud-top entrainment can be very weak if the air overlying the fog is nearly saturated, while it can be as strong as the surface flux term if the air is dry. All these processes counteract the production of LWP by radiative cooling at fog top.

Our sensitivity study indicates that the presence of liquid water on top of the surface is important for the fog LWP budget. Even with saturated soil, in the simulation without initial liquid on the surface the fog dissipates 85 min earlier than in the simulation where the initial fraction of surface covered by liquid is 50%. This is because the loss of LWP by surface fluxes is very sensitive to the Bowen ratio. A dry

surface therefore causes a lower fog LWP, while not affecting the cloud-top height, thereby triggering an earlier fog dissipation.

The profiles of humidity and temperature in the layer right above the fog top have a significant impact on fog dissipation time. If the humidity in this layer is low, it can accelerate fog dissipation through its evaporative effect when mixing with the fog; dissipation is 70 min earlier in the run with dry air above than in the run where the air above is close to saturation. However, as the humidity also affects radiative cooling, the effect of a dry atmosphere aloft will depend on the details of the humidity profile. The simulated fog develops vertically much faster when the layer above is weakly stratified, thereby causing a dissipation by lifting of the fog base 90 min earlier in the run with weak stratification than in the Baseline run which has stronger stratification. Thus, in this case it is the faster increase in the cloud-top height which allows an earlier dissipation, while the LWP is actually higher than in Baseline. This shows that the evolutions of both the cloud-top height and the LWP are important for fog dissipation at the surface. Since entrainment appears as a major driver of fog dissipation, it is important to consider the sensitivity of the entrainment velocity to the numerical schemes when modelling fog, an aspect not tested in this paper.

The deposition of droplets appears as a weak sink process (5–10 $g\,m^{-2}\,hr^{-1}$). We related this to the evaporation of the droplets at the first model level due to the heating from the surface after sunrise. However, the real interaction between the fog droplets and the surface will be much more complex, with notably an important impact of canopy height and structure and other vegetation factors (Katata, 2014). To better understand the role of deposition, these aspects need to be modelled, as well as using a more comprehensive microphysics scheme.

Given the large importance of the Bowen ratio, future efforts should be made to better estimate it in fog conditions from measurements, as we found that the eddy covariance method does not give sufficiently accurate measurements to determine the Bowen ratio. In the meantime, the net radiation at the surface, which can be measured with high accuracy, could be used to estimate the turbulent heat fluxes with some assumption on the Bowen ratio or surface resistance and the ground flux fraction. The important impacts of the variability in the stratification and relative humidity directly above fog top suggest that more detailed and continuous observations of this layer could be interesting for understanding and predicting fog. The radiosonde dataset used in this study provides only snapshots of data at midday and midnight, and in addition the humidity sensor might be affected by wetting. A more systematic observation of the layer above would be valuable.

When studying the performance of fog forecasts by numerical weather prediction (NWP) models, attention should be given to how well the model reproduces these above-fog properties, since the quality of fog forecasts is likely sensitive to it. Assimilation of new observations (e.g. microwave radiometer, water vapour lidar) might improve the forecasts by improving the initial temperature and humidity profiles. The analysis method used to study the LWP budget in this paper, which to our knowledge is a novel approach to study model output, could also be applied to other model studies of fog. It could also be applied to columns in 3D NWP models, if all necessary outputs are available, including the advection through the lateral boundaries.

ACKNOWLEDGEMENTS

This research is supported financially by the French Ministry of Defence – Direction Générale de l'Armement – and by the company Meteomodem. GJS acknowledges financial support from NWO contract 863.10.010 (VENI study – Lifting the fog). The authors would like to acknowledge SIRTA for providing the observational data used in this study, obtained in the framework of the ACTRIS-2 project (funded by the European Union's Horizon 2020 research and innovation programme under grant agreement no. 654109). The authors would like to thank the technical and computer staff of the SIRTA Observatory and Trappes Météo-France station for taking the observations and making the dataset easily accessible. We thank KNMI for providing the Cabauw tower data via http://www.cesar-database.nl/ (accessed 17 January 2019). ERA5 data are provided through ECMWF, COPERNICUS Climate Change Service data, available from the ESPRI/IPSL data centre. The numerical simulations were performed with the supercomputer facilities at SURFsara and financially sponsored by the Netherlands Organisation for Scientific Research (NWO) Physical Science Division (project number SH-312-15). The authors benefited from mobility grants from the Wageningen Institute for Environment and Climate Research and the ACTRIS Trans-National Access. We would like to thank Stephan de Roode, Arnold Moene and Fred Bosveld for their help with interpreting our results, and Chiel van Heerwaarden for his help with setting up the DALES model.

ORCID

Eivind G. Wærsted https://orcid.org/0000-0002-8229-5505
Gert-Jan Steeneveld https://orcid.org/0000-0002-5922-8179

REFERENCES

American Meteorological Society (2012) *Glossary of Meteorology*: Fog. http://glossary.ametsoc.org/wiki/Fog; accessed 7 September 2018

Beljaars, A.C. and Bosveld, F.C. (1997) Cabauw data for the validation of land surface parameterization schemes. *Journal of Climate*, 10(6), 1172–1193. https://doi.org/10.1175/1520-0442(1997)010.

Bergot, T. (2013) Small-scale structure of radiation fog: a large-eddy simulation study. *Quarterly Journal of the Royal Meteorological Society*, 139, 1099–1112. https://doi.org/10.1002/qj.2051.

Bergot, T. (2016) Large-eddy simulation study of the dissipation of radiation fog. *Quarterly Journal of the Royal Meteorological Society*, 142, 1029–1040. https://doi.org/10.1002/qj.2706.

Brown, R. and Roach, W.T. (1976) The physics of radiation fog: II – a numerical study. *Quarterly Journal of the Royal Meteorological Society*, 102, 335–354. https://doi.org/10.1002/qj.49710243205.

Campoy, A., Ducharne, A., Cheruy, F., Hourdin, F., Polcher, J. and Dupont, J.C. (2013) Response of land surface fluxes and precipitation to different soil bottom hydrological conditions in a general circulation model. *Journal of Geophysical Research: Atmospheres*, 118(19), 10725–10739.

Conzemius, R.J. and Fedorovich, E. (2006) Dynamics of sheared convective boundary layer entrainment. Part II: evaluation of bulk model predictions of entrainment flux. *Journal of the Atmospheric Sciences*, 63(4), 1179–1199. https://doi.org/10.1175/JAS3696.1.

Cuxart, J., Conangla, L. and Jiménez, M. (2015) Evaluation of the surface energy budget equation with experimental data and the ECMWF model in the Ebro Valley. *Journal of Geophysical Research: Atmospheres*, 120(3), 1008–1022.

Delanoë, J., Protat, A., Vinson, J.-P., Brett, W., Caudoux, C., Bertrand, F., Parent du Chatelet, J., Hallali, R., Barthes, L., Haeffelin, M. and Dupont, J.-C. (2016) BASTA: a 95 GHz FMCW Doppler radar for cloud and fog studies. *Journal of Atmospheric and Oceanic Technology*, 33(5), 1023–1038. https://doi.org/10.1175/JTECH-D-15-0104.1.

de Roode, S.R., Duynkerke, P.G. and Jonker, H.J. (2004) Large-eddy simulation: How large is large enough? *Journal of the Atmospheric Sciences*, 61(4), 403–421. https://doi.org/10.1175/1520-0469(2004)061<0403:LSHLIL>2.0.CO;2.

Dupont, J., Haeffelin, M., Stolaki, S. and Elias, T. (2016) Analysis of dynamical and thermal processes driving fog and quasi-fog life cycles using the 2010–2013 Parisfog dataset. *Pure and Applied Geophysics*, 173(4), 1337–1358. https://doi.org/10.1007/s00024-015-1159-x.

ECMWF. (2016) IFS Documentation Cy43r1, Part IV: Physical Processes. ECMWF, Reading, UK.

Egli, S., Maier, F., Bendix, J. and Thies, B. (2015) Vertical distribution of microphysical properties in radiation fogs – a case study. *Atmospheric Research*, 151, 130–145.

Elias, T., Haeffelin, M., Drobinski, P., Gomes, L., Rangognio, J., Bergot, T., Chazette, P., Raut, J.-C. and Colomb, M. (2009) Particulate contribution to extinction of visible radiation: pollution, haze, and fog. *Atmospheric Research*, 92(4), 443–454. https://doi.org/10.1016/j.atmosres.2009.01.006.

Fesquet, C., Drobinski, P., Barthlott, C. and Dubos, T. (2009) Impact of terrain heterogeneity on near-surface turbulence structure. *Atmospheric Research*, 94(2), 254–269. https://doi.org/10.1016/j.atmosres.2009.06.003.

Foken, T. (2008) The energy balance closure problem: an overview. *Ecological Applications*, 18(6), 1351–1367. https://doi.org/10.1890/06-0922.1.

Fox, N.I. and Illingworth, A.J. (1997) The retrieval of stratocumulus cloud properties by ground-based cloud radar. *Journal of Applied Meteorology*, 36(5), 485–492. https://doi.org/10.1175/1520-0450(1997)036<0485:TROSCP>2.0.CO;2.

Garratt, J.R. (1992) *The Atmospheric Boundary Layer*. Cambridge: Cambridge University Press.

Gultepe, I., Tardif, R., Michaelides, S.C., Cermak, J., Bott, A., Bendix, J., Müller, M.D., Pagowski, M., Hansen, B., Ellrod, G., Jacobs, W., Toth, G. and Cober, S.G. (2007) Fog research: a review of past achievements and future perspectives. *Pure and Applied Geophysics*, 164(6–7), 1121–1159. https://doi.org/10.1007/s00024-007-0211-x.

Gultepe, I., Pearson, G., Milbrandt, J.A., Hansen, B., Platnick, S., Taylor, P., Gordon, M., Oakley, J.P. and Cober, S.G. (2009) The fog remote sensing and modeling field project. *Bulletin of the American Meteorological Society*, 90(3), 341–359. https://doi.org/10.1175/2008BAMS2354.1.

Haeffelin, M., Barthès, L., Bock, O., Boitel, C., Bony, S., Bouniol, D., Chepfer, H., Chiriaco, M., Cuesta, J., Delanoë, J., Drobinski, P., Dufresne, J.-L., Flamant, C., Grall, M., Hodzic, A., Hourdin, F., Lapouge, F., Lemaître, Y., Mathieu, A., Morille, Y., Naud, C., Noël, V., O'Hirok, B., Pelon, J., Pietras, C., Protat, A., Romand, B., Scialom, G. and Vautard, R. (2005) SIRTA, a ground-based atmospheric observatory for cloud and aerosol research. *Annales Geophysicae*, 23, 253–275. https://doi.org/10.5194/angeo-23-253-2005.

Haeffelin, M., Bergot, T., Elias, T., Tardif, R., Carrer, D., Chazette, P., Colomb, M., Drobinski, P., Dupont, E., Dupont, J.C., Gomes, L., Musson-Genon, L., Pietras, C., Plana-Fattori, A., Protat, A., Rangognio, J., Raut, J.-C., Rémy, S., Richard, D., Sciare, J. and Zhang, X. (2010) PARISFOG: shedding new light on fog physical processes. *Bulletin of the American Meteorological Society*, 91(6), 767–783. https://doi.org/10.1175/2009BAMS2671.1.

Haeffelin, M., Laffineur, Q., Bravo-Aranda, J.-A., Drouin, M.-A., Casquero-Vera, J.-A., Dupont, J.-C. and De Backer, H. (2016) Radiation fog formation alerts using attenuated backscatter power from automatic lidars and ceilometers. *Atmospheric Measurement Techniques*, 9(11), 5347–5365. https://doi.org/10.5194/amt-9-5347-2016.

Haiden, T., Janousek, M. and Hersbach, H. (2017) ERA5 aids in forecast performance monitoring. *ECMWF Newsletter*, 150, 8–8.

Heus, T., Van Heerwaarden, C.C., Jonker, H.J., Siebesma, A.P., Axelsen, S., Van Den Dries, K., Geoffroy, O., Moene, A.F., Pino, D., de Roode, S.R. and Vilà-Guerau de Arellano, J. (2010) Formulation of the Dutch Atmospheric Large-Eddy Simulation (DALES) and overview of its applications. *Geoscientific Model Development*, 3(2), 415–444. https://doi.org/10.5194/gmd-3-415-2010.

Jacobs, A.F., Heusinkveld, B.G., Wichink Kruit, R.J. and Berkowicz, S.M. (2006) Contribution of dew to the water budget of a grassland area in the Netherlands. *Water Resources Research*, 42(3). https://doi.org/10.1029/2005WR004055.

Jarvis, P. (1976) The interpretation of the variations in leaf water potential and stomatal conductance found in canopies in the field. *Philosophical Transactions of the Royal Society of London, Series B, Biological Sciences*, 273(927), 593–610.

Katata, G. (2014) Fogwater deposition modeling for terrestrial ecosystems: a review of developments and measurements. *Journal of Geophysical Research: Atmospheres*, 119(13), 8137–8159. https://doi.org/10.1002/2014JD021669.

Khairoutdinov, M. and Kogan, Y. (2000) A new cloud physics parameterization in a large-eddy simulation model of marine stratocumulus. *Monthly Weather Review*, 128(1), 229–243. https://doi.org/10.1175/1520-0493(2000)128<0229:ANCPPI>2.0.CO;2.

Kotthaus, S., O'Connor, E., Münkel, C., Charlton-Perez, C., Haeffelin, M., Gabey, A.M. and Grimmond, C.S.B. (2016) Recommendations for processing atmospheric attenuated backscatter profiles from Vaisala CL31 ceilometers. *Atmospheric Measurement Techniques*, 9(8), 3769–3791. https://doi.org/10.5194/amt-9-3769-2016.

Leuning, R., Van Gorsel, E., Massman, W.J. and Isaac, P.R. (2012) Reflections on the surface energy imbalance problem. *Agricultural and Forest Meteorology*, 156, 65–74. https://doi.org/10.1016/j.agrformet.2011.12.002.

Maalick, Z., Kühn, T., Korhonen, H., Kokkola, H., Laaksonen, A. and Romakkaniemi, S. (2016) Effect of aerosol concentration and absorbing aerosol on the radiation fog life cycle. *Atmospheric Environment*, 133, 26–33. https://doi.org/10.1016/j.atmosenv.2016.03.018.

Marke, T., Ebell, K., Löhnert, U. and Turner, D.D. (2016) Statistical retrieval of thin liquid cloud microphysical properties using ground-based infrared and microwave observations. *Journal of Geophysical Research: Atmospheres*, 121(24), 14558–14573. https://doi.org/10.1002/2016JD025667.

Maronga, B. and Bosveld, F. (2017) Key parameters for the life cycle of nocturnal radiation fog: a comprehensive large-eddy simulation study. *Quarterly Journal of the Royal Meteorological Society*, 143, 2463–2480. https://doi.org/10.1002/qj.3100.

Mazoyer, M. (2016) *Impact du processus d'activation sur les propriétés microphysiques des brouillards et sur leur cycle de vie*. PhD thesis. Institut National Polytechnique de Toulouse, France

Mazoyer, M., Lac, C., Thouron, O., Bergot, T., Masson, V. and Musson-Genon, L. (2017) Large-eddy simulation of radiation fog: impact of dynamics on the fog life cycle. *Atmospheric Chemistry and Physics*, 17(21), 13017–13035. https://doi.org/10.5194/acp-17-13017-2017.

Nakanishi, M. (2000) Large-eddy simulation of radiation fog. *Boundary-Layer Meteorology*, 94(3), 461–493. https://doi.org/10.1023/A:1002490423389.

Pasini, A., Pelino, V. and Potestà, S. (2001) A neural network model for visibility nowcasting from surface observations: results and sensitivity to physical input variables. *Journal of Geophysical Research: Atmospheres*, 106(D14), 14951–14959. https://doi.org/10.1029/2001JD900134.

Penman, H.L. (1948) Natural evaporation from open water, bare soil and grass. *Proceedings of the Royal Society of London, Series A, Mathematical and Physical Sciences*, 193(1032), 120–145.

Porson, A., Price, J.S., Lock, A.P. and Clark, P.A. (2011) Radiation fog. Part II: large-eddy simulations in very stable conditions. *Boundary-Layer Meteorology*, 139(2), 193–224. https://doi.org/10.1007/s10546-010-9579-8.

Price, J.S., Porson, A. and Lock, A.P. (2015) An observational case study of persistent fog and comparison with an ensemble forecast model. *Boundary-Layer Meteorology*, 155(2), 301–327.

Price, J.S. (1991) Evaporation from a blanket bog in a foggy coastal environment. *Boundary-Layer Meteorology*, 57(4), 391–406. https://doi.org/10.1007/BF00120056.

Román-Cascón, C., Steeneveld, G., Yagüe, C., Sastre, M., Arrillaga, J. and Maqueda, G. (2016) Forecasting radiation fog at climatologically contrasting sites: evaluation of statistical methods and WRF. *Quarterly Journal of the Royal Meteorological Society*, 142, 1048–1063. https://doi.org/10.1002/qj.2708.

Spuler, S., Repasky, K., Morley, B., Moen, D., Hayman, M. and Nehrir, A. (2015) Field-deployable diode-laser-based differential absorption lidar (DIAL) for profiling water vapor. *Atmospheric Measurement Techniques*, 8(3), 1073–1087. https://doi.org/10.5194/amt-8-1073-2015.

Steeneveld, G.J., Ronda, R.J. and Holtslag, A.A.M. (2015) The challenge of forecasting the onset and development of radiation fog using mesoscale atmospheric models. *Boundary-Layer Meteorology*, 154(2), 265–289. https://doi.org/10.1007/s10546-014-9973-8.

Stevens, B. (2002) Entrainment in stratocumulus-topped mixed layers. *Quarterly Journal of the Royal Meteorological Society*, 128, 2663–2690. https://doi.org/10.1256/qj.01.202.

Tanré, D., Deroo, C., Duhaut, P., Herman, M., Morcrette, J., Perbos, J. and Deschamps, P. (1990) Technical note description of a computer code to simulate the satellite signal in the solar spectrum: the 5S code. *International Journal of Remote Sensing*, 11(4), 659–668. https://doi.org/10.1080/01431169008955048.

Tardif, R. and Rasmussen, R.M. (2007) Event-based climatology and typology of fog in the New York City region. *Journal of Applied Meteorology and Climatology*, 46(8), 1141–1168. https://doi.org/10.1175/JAM2516.1.

Van der Dussen, J., de Roode, S.R. and Siebesma, A.P. (2014) Factors controlling rapid stratocumulus cloud thinning. *Journal of the Atmospheric Sciences*, 71(2), 655–664. https://doi.org/10.1175/JAS-D-13-0114.1.

Van Ulden, A. and Holtslag, A. (1985) Estimation of atmospheric boundary layer parameters for diffusion applications. *Journal of Climate and Applied Meteorology*, 24(11), 1196–1207. https://doi.org/10.1175/1520-0450(1985)024<1196:EOABLP>2.0.CO;2.

Wærsted, E.G., Haeffelin, M., Dupont, J.-C., Delanoë, J. and Dubuisson, P. (2017) Radiation in fog: quantification of the impact on fog liquid water based on ground-based remote sensing. *Atmospheric Chemistry and Physics*, 17(17), 10811–10835. https://doi.org/10.5194/acp-17-10811-2017.

How to cite this article: Wærsted EG, Haeffelin M, Steeneveld G-J, Dupont J-C. Understanding the dissipation of continental fog by analysing the LWP budget using idealized LES and *in situ* observations. *Q J R Meteorol Soc*. 2019;145:784–804. https://doi.org/10.1002/qj.3465

APPENDICES

A: MODIFICATIONS TO THE DALES CODE

Here follows a list of the modifications made to the DALES code:

- The calculation of the solar zenith angle is performed more accurately with the algorithm used in the 5S solar radiation code (Tanré *et al.*, 1990).
- The parameter SW_0 (sw0) varies with solar zenith angle (Table 2).
- The DSD is made consistent between the SW radiation scheme and the bulk microphysics scheme by calculating in each grid cell the effective radius r_e (used in the SW scheme) from the parameters N_c and σ_{gc} (Table 2) and current LWC, rather than using a constant value (ρ_l is liquid water density):

$$r_e{}^3 = \frac{3LWC}{4\pi\rho_l N_c} e^{3\ln^2\sigma_{gc}}. \tag{A1}$$

- In the SW scheme, the extinction coefficient is increased by $0.01\ \mathrm{m}^{-1}$ in grid cells with cloud water to account for hydrated unactivated aerosols.
- At the first model level, a turbulent deposition flux, proportional to the LWC at this model level, is added: $F_{dep} = V_d LWC$, where $V_d = 0.02$ m/s. The water is moved from the first model level to the surface liquid reservoir.
- Sedimentation fluxes at the first model level feed the surface liquid reservoir (this was not included in the original code).
- Sedimentation fluxes are written as model output.
- Adjustments of the interface between the surface module and radiation module to make it work correctly when using the parametrized radiation scheme (which has different conventions for the model fields than the full radiation scheme)
- Correction of a bug that prevented the broadcasting of the variables N_c (Nc_0) and σ_{gc} (sig_g) to all computation cores

B: LWP BUDGET TERMS FROM MODEL OUTPUT

This appendix explains how we calculate the SH, LH and F_{liq} fluxes in Equations 5, 7, 8 from the model output. They are all calculated from the horizontal and temporal mean profiles of state variables and fluxes that are provided as model output every 5 min. We consider the fog to be contained between the current mean CBH and CTH in the model, which are also given in the output.

Since only the cloud interacts with radiation in the simplified parametrizations used in the model (section 3.1), SH_{LW} and SH_{SW} are calculated by subtracting the net downward irradiance at the surface from the net downward irradiance at the top of the domain. The adiabatic heating from subsidence is calculated using the adiabatic lapse rate (g/c_p) and the constant vertical gradient in large-scale vertical velocity ($\mathrm{d}w_{ls}/\mathrm{d}z$):

$$\begin{aligned} SH_{sub} &= \int_{CBH}^{CTH} \rho_a c_p \frac{g}{c_p}(-w_{ls})\,\mathrm{d}z \\ &= \frac{1}{2}\rho_a g\left(-\frac{\mathrm{d}w_{ls}}{\mathrm{d}z}\right)\left(CTH^2 - CBH^2\right), \end{aligned} \tag{B1}$$

where $g = 9.81\ \mathrm{m/s}^2$ is the acceleration of gravity.

The interactions between the fog and the layers below and above have contributions from sensible heat, latent heat and liquid fluxes. These are taken directly from the model profile output at the model interface closest to the current mean CBH and CTH. At the upper boundary, we combine all the fluxes to

the term named "entrainment". This entrainment term is more challenging to quantify from the model output than the other terms, due to the horizontal heterogeneity of CTH and the increase of CTH with time. The inclusion a new level means that the liquid already present at this level and its degree of non-saturation need to be taken into account. The latter is considered as a negative latent heat flux. In addition, the large-scale subsidence will transport some of the air from the layer above cloud top into the cloud. To account for all of these effects, the total expressions for the entrainment fluxes are:

$$SH_{\text{top}} = -\rho_{\text{a,top}}\, c_p\, \overline{w'\theta'}_{\text{top}}\,, \tag{B2}$$

$$LH_{\text{top}} = -\rho_{\text{a,top}}\, L_{\text{v}}\, \overline{w'q'_{\text{v}}}_{\text{top}} - (-w_{\text{ls,ab}})\rho_{\text{a,ab}} L_{\text{v}} \left\{ q_{\text{s}}(T_{\text{ab}}) - q_{\text{v,ab}} \right\} - \sum_j \rho_{\text{a},j} L_{\text{v}} \{ q_{\text{s}}(T_j) - q_{\text{v},j} \} \frac{\Delta h_j}{\Delta t}\,, \tag{B3}$$

$$F_{\text{liq,top}} = -\rho_{\text{a,top}} \overline{w'q'_{\text{liq,top}}} + (-w_{\text{ls,ab}}) LWC_{\text{ab}} + \sum_j LWC_j \frac{\Delta h_j}{\Delta t} + F_{\text{sed,top}}\,. \tag{B4}$$

The overlined expressions are the turbulent kinematic vertical fluxes of sensible heat, specific humidity and specific liquid water content (i.e. LWC/ρ_a) at the current CTH. The sums go over the model levels above CTH which are added to the fog layer between the current and the next output time. Δt is the time between two output times (5 min), and Δh_j, T_j $q_{v,j}$, $\rho_{a,j}$ and LWC_j are the thickness, temperature, specific humidity, density and LWC, respectively, of the model level being added. F_{sed} is the downward flux of LWC due to sedimentation. q_{s} is the saturation specific humidity. Subscript $_{\text{top}}$ indicates the first model level above CTH, and $_{\text{ab}}$ the next level above this (from which the subsidence velocity is transporting the properties across CTH, assuming $w_{\text{ls}} < 0$). The first term in SH_{top} (LH_{top}) represents the turbulent sensible (latent) heat flux across the current CTH. The second term in LH_{top} accounts for the subsaturation introduced by subsidence transport, and the third term is the subsaturation in the added model levels due to vertical development of CTH. The terms of $F_{\text{liq,top}}$ represent, respectively, the turbulent liquid transport across the current CTH, the transport by large-scale subsidence across current CTH, the liquid already present in layers being added to the fog as it develops vertically, and the sedimentation flux (of cloud water and rainwater) across the current CTH.

Figure B1 shows the relative importance of all these contributions to the entrainment term in the LWP budget equation in Figure 10. The total entrainment term is a difference between positive and negative contributions that are similar in magnitude (apart from the subsidence terms, which are weak), the most important terms being the (Eulerian) turbulent fluxes of heat, water vapour and liquid. Due to the large gradients in temperature and humidity at the non-flat cloud top, the precision of these flux estimates is limited. Recognising that the entrainment term is most likely the main source of the residual in the LWP budget, at least until fog dissipation, we have chosen to deduce the entrainment term from the closure of the LWP budget rather than calculating it in Figure 12.

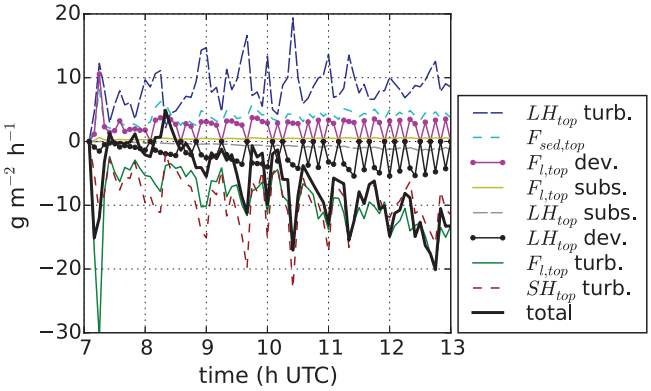

FIGURE B1 The contribution of each term in Equations B2, B3, B4 to the entrainment term in the fog LWP budget (Table 4, Figure 10), in the Baseline simulation

At the lower boundary, the terms SH_{base}, LH_{base} and $F_{\text{liq,base}}$ are calculated in a similar way as for the top, except that the effect of subsidence is neglected and that levels are being removed instead of added. In Figure 10, we also consider sedimentation and turbulent liquid fluxes separately. The expressions are:

$$SH_{\text{base}} = \rho_{\text{a,base}} c_p \overline{w'\theta'}_{\text{base}}, \tag{B5}$$

$$LH_{\text{base}} = \rho_{\text{a,base}} L_{\text{v}} \overline{w'q'_{\text{v}}}_{\text{base}}, \tag{B6}$$

$$F_{\text{liq,base,Sed}} = -F_{\text{sed,base}}, \tag{B7}$$

$$F_{\text{liq,base,Turb}} = \rho_{\text{a,top}} \overline{w'q'_{\text{liq}}}_{\text{base}} - \sum_j LWC_j \frac{\Delta h_j}{\Delta t}. \tag{B8}$$

In Equation B8, the sum goes over the layers being removed from the fog as CBH rises. However, until the mean CBH lifts to 4 m, we let the lower boundary ("base") be at the surface, so that the fluxes from below correspond to the surface–atmosphere interaction, which is parametrized with Monin–Obukhov similarity theory (for SH_{base}, LE_{base}) and the parametrized turbulent deposition (for $F_{\text{liq,base,Turb}}$). Once the CBH has lifted to above 4 m (our definition of fog dissipation), the fluxes correspond to the interaction between two atmosphere layers, which is governed by the model interior dynamics. This is the reason for the discontinuity seen in the terms in Figure 10 at fog dissipation.